RESEARCH ARTICLE | OCTOBER 02 2025

Computational fluid dynamics of polymer flow-induced crystallization using the polySTRAND model •

W. P. Grant (10); O. G. Harlen (12); D. J. Read (10)



J. Rheol. 69, 905-923 (2025)

https://doi.org/10.1122/8.0000999





Related Content

Experimental observations and matching viscoelastic specific work predictions of flow-induced crystallization for molten polyethylene within two flow geometries

J. Rheol. (July 2009)

Nonlinear rheology of polydisperse blends of entangled linear polymers: Rolie-Double-Poly models

J. Rheol. (January 2019)

Rheo-Optic Flow-induced Crystallization of Polyethylene and Polypropylene within Confined Flow Geometries

AIP Conf. Proc. (July 2008)



Anton PaarRheology Without Limits







Computational fluid dynamics of polymer flow-induced crystallization using the polySTRAND model

W. P. Grant, O. G. Harlen, and D. J. Read

¹School of Chemical and Process Engineering, University of Leeds, Leeds LS2 9JT, United Kingdom ²School of Mathematics, University of Leeds, Leeds LS2 9JT, United Kingdom

(Received 24 February 2025; final revision received 20 August 2025; published 2 October 2025)

Abstract

A computational model for predicting regions of flow-induced crystallization (FIC) during processing of a polydisperse polymer melt is presented. Flow produces local alignment of polymer segments that reduces the energy barrier for nucleation, which can lead to a dramatic increase in the rate of formation of crystal nuclei. However, simulating FIC in a complex flow geometry is challenging due to the need to couple a molecular-level description of chain configuration to the macroscale flow dynamics. This is compounded in polydisperse melts as the most marked flow-induced effects occur from the long-chain species at low undercooling. In this work, we use the Rolie-Double-Poly (RDP) model [Boudara *et al.*, J. Rheol. **63**, 71–91 (2019)] in combination with the polySTRAND model [Read *et al.*, Phys. Rev. Lett. **124**, 147802 (2020)] to create a computationally viable method for modeling FIC. This model is used to examine flow-induced crystallization in a contraction-expansion geometry, where previous experiments [Scelsi *et al.*, J. Rheol. **53**, 859–876 (2009)] found a highly localized region of crystal formation at and downstream of the wall of the constriction. © *2025 Author(s)*. *All article content, except where otherwise noted, is licensed under a Creative Commons Attribution (CC BY) license (https://creativecommons.org/licenses/by/4.0/)*. https://doi.org/10.1122/8.0000999

I. INTRODUCTION

The modeling of flow-induced crystallization (FIC) of polymers is important for controlling industrial processes. Flow dramatically enhances the nucleation rate, which strongly affects the crystal morphology. The ability to model FIC effectively could significantly improve the efficiency of polymer processing by allowing the final crystal structure to be determined by tailoring the processing conditions to suit.

A significant challenge in studying crystallization in polymers is the wide range of length and time scales involved. The formation of a crystal nucleus is an extremely rapid and highly localized event that cannot be directly observed experimentally [1]. However, with small-angle x-ray scattering (SAXS) [2–6], it is now possible to track the formation of shish-kebab crystals, as well as determining the pre-factors for their development.

Molecular dynamics (MD) simulations do provide a means to study flow-induced nucleation (FIN) by resolving nucleation events from simulations of polymer moderately entangled polymer chains under flow [7–12]. Recent studies have reduced the degree of undercooling that is required for practical simulation [13–20]. Under strong, persistent extensional flow (planar or uniaxial), where chains are extended even below the Kuhn segment scale, crystallisation is strongly accelerated leading to highly stable crystals that persist even above the melting temperature within simulation timescales [21]. There are also now detailed simulations showing the formation

Given this difficulty of reaching the necessary time scales and molecular weights while treating FIC at an atomistic modelling level, it is necessary to turn to coarse-grained approaches. It is hoped that these can capture the essential physics of FIC, i.e., that acceleration of nucleation relates to the flow-induced changes in chain configurations at different scales. At larger scales, crystallization is accompanied by a loss in chain entropy, which contributes to the free energy barrier towards crystal nucleation. Flow leads to stretch and orientation of the chains, which reduces chain entropy, and reduces the change in chain entropy required for crystallization. This effectively reduces the free energy barrier toward nucleation, producing the accelerating effect of FIC. Coarse-grained models for FIC typically capture this by focussing on the chain orientation and alignment at the scale of the Kuhn segment, which is the approach we will adopt here. Some justification for this is found, for example, from the MD simulations of Nicholson and Rutledge [8], who find a strong correlation between the nucleation rate and the Kuhn segment nematic order parameter. On smaller scales, flow can also lead to stretching of the Kuhn segments themselves, changing their internal configurations (e.g., changing the ratio of trans to gauche configurations in PE) so that these internal configurations more closely resemble those within the crystal. To be

of particular crystal morphologies, such as the shish-kebab structure of crystals [16,22]. There are also now some MD studies examining molecular weight distribution in polymer blends and solutions [20,23,24]. However, despite this recent progress, there remains a considerable gap between the time scales and molecular weights of polymers that can be simulated in MD studies and those used in experimental investigations or in industrial processing.

a) Author to whom correspondence should be addressed; electronic mail: o.g.harlen@leeds.ac.uk

[©] Author(s) 2025.

significant, this typically requires strong flows in which forces developed in the chain become of order k_BT/b , where b is the Kuhn segment length. However, in principle, this happens to some extent at all flow rates: Significant alignment at the Kuhn segment level will be accompanied by changes in internal configurations. Capturing such effects in strong flows may require the introduction of further parameters to distinguish alignment and stretching of Kuhn segments, though we do not believe this level of detail has been included in any of the coarse-grained approaches detailed below.

At the highest level of coarse graining, continuum-level models use differential equations [25–28] to describe crystal nucleation and growth. These models use empirical laws to relate the rate of nucleation to a property of the constitutive equation (typically a measure of chain stretch of the largest molecular weight component). For example, van Berlo et al. [29] used the stretch of the longest relaxation time mode of a multimode XPP model [30] to determine the flow-induced nucleation rate of an iPP melt in a filament stretching extensional rheometer (FiSER). Although these models enable simulation of FIC in processing flow conditions, they do not include a detailed description of how the polymer chain conformation controls the rate of nucleation. In particular, they struggle to predict the effects of polydispersity, as the models lack the necessary detail to capture the influence of chain species of different lengths on nucleation. Although longer chains do contribute disproportionately to crystal nuclei, shorter chains typically make up the bulk of the polymer mass and so their contribution cannot necessarily be neglected.

The GO model [31,32] provides an intermediate approach between MD and continuum modelling. The nucleation dynamics are simulated stochastically with a constitutive equation used to describe amorphous chain dynamics. This allows it to access both long chains and low undercooling that cannot be reached in molecular dynamics. The model compares well with experiments [32,33]. However, this model is still computationally too expensive to be used for simulations of processing flows [1] where there is spatial variation in the nucleation rate.

The polySTRAND model [34] directly addresses the challenge of providing a model for flow-induced nucleation that is simple enough to be used in processing flow simulations, but that is directly linked to the molecular origins of crystal nucleation in polymers. It uses insights from both molecular dynamics (MD) and kinetic Monte Carlo simulations within the framework of thermodynamic modeling to provide a continuum-level model for FIC in polymers. The effect of polydispersity on both flow and nucleation dynamics is accounted for: in particular, longer chains deform strongly so attach more readily than shorter less deformed chains. This long-chain enrichment that is predicted by the polySTRAND model was confirmed in a recent MD investigation by Anwar et al. [20] where they found good agreement between their MD simulation results for long-chain enrichment and the calculations of the polySTRAND model.

All of these coarse-grained models require a constitutive model that describes the conformation of the polymer chains. Doufas *et al.* [25] used a modified Giesekus model, whereas Steenbakkers and Peters [26] and McIlroy and Graham [28]

both use the Rolie-Poly model [35]. All of the above models consider a single chain species and so do not distinguish between chains of different lengths in a polydisperse blend. A recent constitutive equation that accounts for polydispersity is the Rolie-Double-Poly (RDP) model [36]. The RDP model accounts for linear and nonlinear couplings between chain species. This allows for accurate predictions of the rheology of polydisperse polymer melts. The RDP model is a highly simplified version of the work done by Read *et al.* [37] for bidisperse materials and results in a model that is computationally cheap and tractable for computational fluid dynamics (CFD) simulations.

The aim of this work is to provide a computationally tractable model for flow-induced crystallization during processing of a polydisperse polymer blend. The RDP model [36] is used to model the flow of the polymer chains, while the polySTRAND model [34] is used to calculate the crystal nucleation rate under flow conditions. An additional benefit to using the polySTRAND model is that it requires parameters that are independent of MWD. Therefore, the polySTRAND model can effectively predict FIC for the same polymeric materials with different MWD using the same set of parameters. The subsequent crystal growth is described by the Schneider rate equations [38].

The paper is organized as follows. In Secs. II and III, we give details of the theory behind both the RDP model and the polySTRAND model and how we obtained appropriate values for the parameters in these models. This then leads into how we implement these models in our investigation. The simulations were carried out in software rheoTool [39], which is a toolbox within open-soure software openFOAM [40]. We then outline the geometry used for the investigation, which was chosen to show agreement with the experiments of our investigation where we look at different flow rates and how these affect the crystallization dynamics at play in the geometry.

II. POLYDISPERSE ROLIE-DOUBLE-POLY MODEL

We use the RDP model [36] to describe the polymer melt flow, as it is appropriate for blends of entangled linear polymers. The RDP model has been successfully implemented within openFOAM for a bi-disperse blend in the work by Azahar $et\ al.$ [42]. In our work, we generalize the openFOAM implementation to include n interacting chain species.

In the RDP model [36], the polymer stress τ_P is the sum of the stress contributions coming from the local average conformation of each species \mathbf{A}_i weighted by their volume fraction ϕ_i and the finite extensibility function $f_E(\lambda_i)$,

$$\boldsymbol{\tau}_P = G_N^0 \sum_{i=1}^n \phi_i f_E(\lambda_i) \mathbf{A}_i \quad \text{with} \quad \lambda_i = \left(\frac{1}{3} \operatorname{Tr} \mathbf{A}_i\right)^{\frac{1}{2}}.$$
 (1)

Here, G_N^0 is the plateau modulus. The stretching ratio λ_i is the ratio of the current tube path length to the equilibrium path length for chain species i. The finite extensibility

function $f_E(\lambda)$ is required to prevent chains stretching beyond their maximum extension λ_{max} . The original RDP model used the Warner approximation [43] for $f_E(\lambda)$, but here we use the normalized Cohen approximation [44],

$$f_E(\lambda) = \left(\frac{3 - \lambda^2 / \lambda_{\text{max}}^2}{1 - \lambda^2 / \lambda_{\text{max}}^2}\right) \left(\frac{1 - 1 / \lambda_{\text{max}}^2}{3 - 1 / \lambda_{\text{max}}^2}\right). \tag{2}$$

This is based on a more accurate Padé approximant to the inverse Langevin function force law for a freely jointed chain. We also use the freely jointed chain model below to calculate bond orientation, so using the more accurate Cohen approximation gives a consistent description. We assume the maximum stretch ratio is given by $\lambda_{\text{max}}^2 = N_e$, where N_e is the number of steps per entanglement segment.

The average conformation tensor, A_i , accounts for the stresses that come from the interaction of the species i with itself and the other (n-1) species; therefore,

$$\mathbf{A}_{i} = \sum_{j=1}^{n} \phi_{j} \mathbf{A}_{ij}, \tag{3}$$

where A_{ij} is the stress conformation tensor on the *i* chains coming from their entanglements with the j chains. This conformation tensor evolves as

$$\mathbf{A}_{ij}^{\nabla} = -\frac{1}{\tau_{d,i}}(\mathbf{A}_{ij} - \mathbf{I}) - \frac{2}{\tau_{s,i}} \left(1 - \frac{1}{\lambda_i} \right) f_E(\lambda_i) \mathbf{A}_{ij} - (\mathbf{A}_{ij} - \mathbf{I}) \left[\frac{\beta_{th}}{\tau_{d,j}} + 2\beta_{CCR} \frac{f_E(\lambda_j)}{\tau_{s,j}} \left(1 - \frac{1}{\lambda_j} \right) \lambda_i^{2\delta} \right], \quad (4)$$

where $\tau_{d,i}$ is the reptation relaxation time and $\tau_{s,i}$ is the stretch relaxation time for each species. The parameter β_{th} is the thermal constraint release coefficient, which we set as $\beta_{th} = 1$ in this work. This coefficient accounts for constraint release relaxation of species i due to the reptation of j chains. In the linear rheology limit, the relaxation rate of the ij mode is the sum of the rates $1/\tau_{d,i}$ and $1/\tau_{d,j}$ from i and j chains, respectively. Therefore, the model is consistent with double reptation theory [45], which models the relaxation of two entanglements, where each entanglement involves an interaction between chains of different lengths.

A key feature of this model is that the n^2 individual conformation tensors A_{ii} are coupled via the terms involving the stretch variables λ_i and λ_i , and therefore, this model cannot be incorporated using the multimode formalism in RheoTool, which is based on a linear superposition of uncoupled modes. As a consequence, it is necessary to create a stand-alone RDP model in which all n^2 modes are individually represented. Although explicitly coding the equations for each conformation tensor is viable for a small number of modes, such as in a bimodal blend for a larger numbers of chain species, it is desirable to have an automated means for coding these equations. To achieve this, we use a script to automatically generate the requisite openFOAM files for the RDP constitutive equations with the desired value of n. The script used to achieve this is available in the Leeds Data Repository, https://doi.org/ 10.5518/1581 [46].

Since the RDP model is based on double reptation [45], the linear relaxation modulus is given by

$$G(t) = G_N^0 \sum_{i=0}^n \sum_{j=0}^n \phi_i \phi_j e^{-t(1/\tau_{d,i} + 1/\tau_{d,j})}.$$
 (5)

Here, the chains are ordered so that i = n corresponds to the longest and slowest chain species, and an additional "0" species has been included to represent fast relaxing chains for which $\tau_{d,0}$ is small compared to the flow time scale and inverse shear rates. This species acts effectively as a solvent, so it is not explicitly modelled using the RDP equations. With these fast relaxing chains included in the summation, the prefactor G_N^0 is the plateau modulus, and ϕ_i represents the volume fraction of each species, including the short chains.

Equation (5) is equivalent to a relaxation spectrum consisting of n(n+1)/2 Maxwell modes. Rearranging Eq. (5) as

$$G(t) = \sum_{i=0}^{n} G_N^0 \phi_i \left(\phi_i e^{-2t/\tau_{d,i}} + 2 \sum_{j>i}^{n} \phi_j e^{-t(\tau_{d,i} + \tau_{d,j})/\tau_{d,i}\tau_{d,j}} \right),$$
(6)

it can be seen that the relaxation times of modes corresponding to the interactions of the *i* chains with *j* chains with $j \ge i \stackrel{\circ}{\circ}$ all lie between $\tau_{d,i}/2$ and $\tau_{d,i}$, so all have similar relaxation $\stackrel{\circ}{\circ}$ times. From Eq. (6), the sum of the elastic moduli for these modes is given by

$$g_i = G_N^0 \left(\phi_i^2 + 2\phi_i \left(\sum_{j>i} \phi_j \right) \right). \tag{7}$$

We call the set of modes corresponding to the interactions of the *i* chains with *j* chains with $j \ge i$, the *i*th "RDP Maxwell mode," because although not strictly identical in relaxation time, they are sufficiently close for practical use. It can readily be observed that the number of RDP Maxwell modes corresponds to the number, n, of RDP chain species.

By integrating Eq. (6), we can obtain the viscosity in the form

$$\eta = \sum_{i=0}^{n} \eta_i,\tag{8}$$

where the viscosity contribution of the ith "RDP Maxwell mode" is

$$\eta_i = G_N^0 \left(\frac{\phi_i^2 \tau_{d,i}}{2} + 2\phi_i \left(\sum_{i>i}^n \phi_j \left(\frac{1}{\tau_{d,i}} + \frac{1}{\tau_{d,j}} \right)^{-1} \right) \right).$$
 (9)

In particular taking the limit in which $\tau_{d,0} \to 0$, but $G_N^0 \tau_{d,0}$ is finite, the terms associated with i = 0 reduce to an effective

solvent viscosity

$$\eta_S = \frac{G_N^0 \tau_{d,0} \phi_0}{2} \left[\phi_0 + 4 \sum_{j=1}^n \phi_j \right]. \tag{10}$$

A. Obtaining a RDP fit to experimental linear and nonlinear rheology

In this section, we consider the matching of an RDP model to experimental linear and non-linear rheology data. The flow-induced crystallization experiments of Scelsi *et al.* [41] were performed using the metallocene catalyzed polyethylene referred to as HDB6. Although this polymer contains a degree of long-chain branching and, therefore, the RDP model is not strictly applicable, we nevertheless use these data illustratively.

For the simulations, we use an RDP model with four species (n = 4) that contribute to nonlinear viscoelasticity and enhanced crystal nucleation, together with a fast relaxing mode that acts effectively as a solvent.

The parameter values for the RDP model are obtained from the 11-mode relaxation spectrum used by Scelsi et al. [41] grouped together to form the four RDP Maxwell modes (as defined above) of our model, by making use of the linear relaxation structure for the RDP model given in Eq. (6). The three longest modes (which formed the stretching Pom-Pom modes [47] in Scelsi model) were combined into the slowest RDP Maxwell mode. The next six modes were combined in pairs to give the next three RDP Maxwell modes. The remaining two shortest modes were included as contributing toward the solvent. However, since the total combined modulus of all Pom-Pom modes in the Scelsi data is less than the plateau modulus of high-density polyethylene, there must be additional solvent contributions arising from shorter time scale modes that are not captured by the 11-mode spectrum of Scelsi et al.

Our strategy (which is applicable to any Maxwell mode fit to linear viscoelastic data) is to match the modulus g_i and viscosity η_i of the *i*th RDP Maxwell mode to the summed moduli and viscosities, respectively, of the associated combined Pom-Pom (Maxwell) modes. This gives us sufficient information to fit the volume fraction, ϕ_i , and the reptation relaxation times, $\tau_{d,i}$, for the respective RDP species (given the one-to-one correspondence between RDP chain species and RDP Maxwell modes).

This strategy is represented in Fig. 1, which shows how each of the RDP (double reptation) modes contributes to the relaxation spectrum. Each RDP mode (species i entangling with species j) is represented by a small square, with its individual weighting indicated. These RDP modes are summed around the "L"-shaped regions to give the RDP Maxwell modes. The correspondence of the RDP Maxwell mode to the Pom-Pom (Maxwell) modes of Scelsi *et al.* is indicated along the upper line, while their correspondence to RDP chain species is indicated along the right. Further details of how the values of $\tau_{d,i}$ and ϕ_i were calculated are given in the supplementary material.

Having calculated the values for $\tau_{d,i}$ and ϕ_i , we then verified that these values match the linear relaxation data from

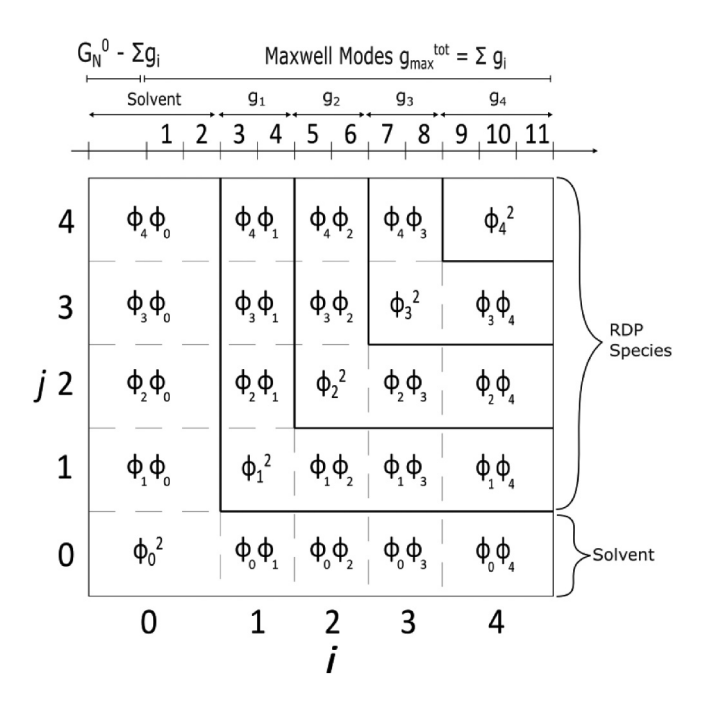


FIG. 1. Diagram showing how the individual contributions from the four-mode RDP model are mapped onto the multimode Maxwell modes used by Scelsi *et al.* [41]. See text for description of figure.

HDB6 [41]. From the computed values of ϕ_i , we calculate the remaining volume fraction $\phi_0 = 1 - \sum \phi_i$, which is treated as a solvent. We obtain an effective relaxation time of this mode by fitting to the high-frequency linear viscoelastic data giving an effective relaxation time of 5×10^{-4} s corresponding to a solvent viscosity of 641 Pa s. The comparison with the measured linear viscoelastic data for HDB6 vover the frequency range from 10^{-2} to 10^2 s⁻¹ is given in Fig. 2. Here, we show the predictions using the original Maxwell mode spectrum of Scelsi *et al.* [41] as given in Table S1 of the supplementary material: This gives a perfect description of the data. We also show the predictions from our RDP model. Here, it is evident that there is a good match to the data, but the process of grouping the Maxwell modes together into just four RDP Maxwell modes gives a slightly

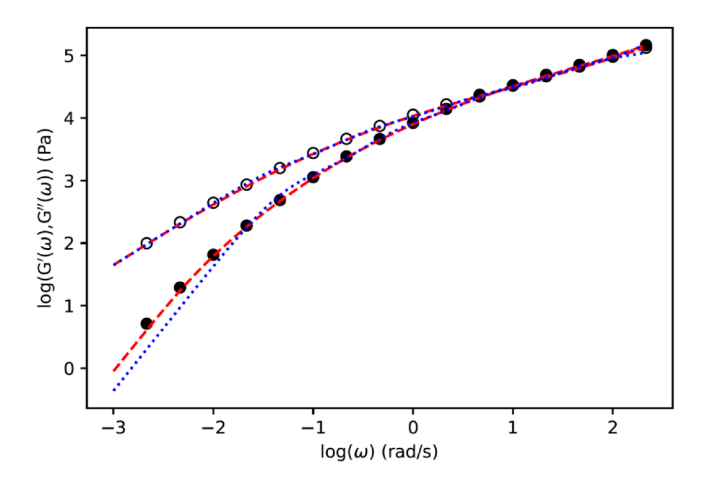


FIG. 2. Figure comparing the measured loss and storage moduli of HDB6 (points and circles) at $155\,^{\circ}\text{C}$ with the original Maxwell mode spectrum of Scelsi *et al.* [41] (dashes) and our predictions from our RDP model (dots).

TABLE I. Table showing the volume fractions and relaxation times that were calculated to match the HDB6 rheology at 155 °C from Ref. [41].

Chain species	ϕ_i	$ au_{d,i}$ s	$ au_{s,i}$ s
Solvent	0.7668	5×10^{-4}	5×10^{-4}
1	0.0936	0.0231	0.01
2	0.0685	0.2323	0.01
3	0.0456	2.296	0.01
4	0.0256	35.7	0.5

worse prediction of the storage modulus, with the largest discrepancy being at low frequency. The loss modulus prediction from the RDP model is almost indistinguishable from the original Maxwell modes, which is a result of matching the viscosities of the lumped modes.

The stretch relaxation times, $\tau_{s,i}$, cannot be obtained from linear rheology but need to be determined from nonlinear rheology. Since we are aiming only at a qualitative comparison with the HDB6 data of Scelsi *et al.* [41], the matching of the HDB6 data will be imperfect. The HDB6 material contains long-chain branches, so the RDP model does not strictly apply. The values in Table I were chosen so that only the longest mode, 4, becomes stretched at the highest shear rates in the simulations and provides an approximate fit to the transient extensional viscosity of HDB6 at $\dot{\varepsilon} = 0.3 \, \text{s}^{-1}$, as shown in Fig. 3. However, as expected, this does not provide a good fit to other extension rates.

All the rheology data for HDB6 [41] were measured at 155 °C, whereas the crystallization experiments were performed at 125 °C. Consequently, to perform calculations at this lower temperature, a time-temperature shift occurs, where all the relaxation times are multiplied by 7.783 [41] and increase the solvent viscosity to 4996 Pa s.

Treating the short chains as a solvent means that they are no longer included explicitly in the RDP model, which has the effect of diluting the polymer concentration. To account for this, it is convenient to renormalize the volume fractions

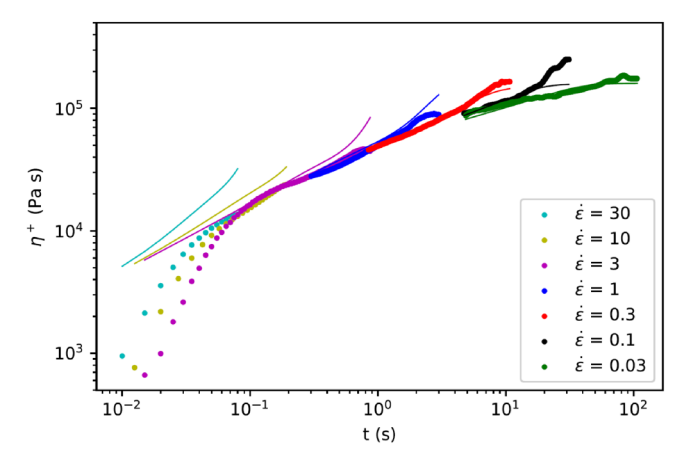


FIG. 3. Comparison of the extensional viscosity, η^+ , for HDB6 (symbols) with the predictions from our RDP model (lines) at T = 155 °C. It should be noted that our model is not intended to provide a detailed fit to this data but does approximately match the degree of extension hardening at $\dot{\varepsilon}=0.3~{\rm s}^{-1}$. The figure shows the results, from left to right, for $\dot{\varepsilon}=30~{\rm s}^{-1}$, $\dot{\varepsilon}=10~{\rm s}^{-1}$, $\dot{\varepsilon}=30~{\rm s}^{-1}$, $\dot{\varepsilon}=10~{\rm s}^{-1}$, and $\dot{\varepsilon}=0.03~{\rm s}^{-1}$.

TABLE II. Table showing the renormalized concentration and relaxation times for each RDP mode used in the simulations at 125 °C along with the renormalized modulus used.

Chain species	$oldsymbol{\phi}_i^*$	$ au_{d,i}$ s	$ au_{s,i}$ s	G_N^* kPa
1	0.401	0.179	0.0778	107
2	0.294	1.81	0.0778	107
3	0.195	17.9	0.0778	107
4	0.110	292	3.89	107

used in the RDP model as

$$\phi_i^* = \frac{\phi_i}{1 - \phi_0},\tag{11}$$

with the renormalized modulus given by

$$G_N^* = (1 - \phi_0)^2 G_N^0. \tag{12}$$

The values for the RDP parameters used in the simulations are summarized in Table II.

III. POLYSTRAND MODEL

The polySTRAND model [34] provides a close analytical approximation to the GO model [31,32] calculation of the rate of crystal nucleation in a flowing polydisperse polymeric ₹ material. The GO model is based on the premise that flowinduced alignment of chain species i produces an additional free energy benefit Δf_i per Kuhn segment for attachment to a \aleph growing nucleus compared to an isotropic orientation. Each g chain species has different degrees of alignment and obtains a different benefit. The GO model uses this to define a Monte Carlo simulation for a growing crystal nucleus, built from the units of the Kuhn segments of the various chain species. In contrast, the polySTRAND model considers the thermodynamic limit of a large number N_T of such Kuhn segments in the growing nucleus and obtains an (almost) analytical expression for the free energy $F(N_T; \{\phi_i\}, \{\Delta f_i\})$ as a function of nucleus size N_T , the free energy benefit Δf_i for each chain species, and their volume fraction ϕ_i in the melt. (The last two steps of the calculation are numerical: a solution of one nonlinear equation and a minimization of resulting free energy over the number of chain strands). This calculation finds that the composition of the nucleus differs from that of the background melt, such that species with more favourable Δf_i are over-represented in the crystal nucleus in terms of both number of chain strands and number of Kuhn segments. Details of this calculation can be found in the original polySTRAND paper [34] and are summarized in the supplementary material.

For a given set of ϕ_i and Δf_i , the free energy barrier toward nucleation, ΔF_{Λ}^* , can be computed as the maximum of $F(N_T; \{\phi_i\}, \{\Delta f_i\})$ with respect to N_T . This free energy barrier affects the rate of nucleation. For the GO model under quiescent conditions (no flow), Hamer *et al.* [48] provided an accurate analytical calculation of the nucleation rate in terms of the relevant time-parameter τ_0 , which is the time scale

associated with Kuhn segment attachment/detachment. The polySTRAND model makes use of this prior work by comparing ΔF_{Λ}^* , calculated under flow conditions with ΔF_q^* , which is the free energy barrier calculated under quiescent conditions with $\Delta f_i = 0$. The nucleation rate under flow is then obtained as

$$\dot{N}_{\Lambda} = \dot{N}_q \exp\left(\Delta F_q^* - \Delta F_{\Lambda}^*\right),\tag{13}$$

where the quiescent nucleation rate \dot{N}_q is found separately using the calculation of Hamer et al. [48]. It was found that, with this procedure, the polySTRAND model predicted nucleation rates in the GO model with a high degree of accuracy, overcoming any approximations resulting from taking the thermodynamic limit.

This calculation gives the nucleation rate per Kuhn step, whereas experiments measure the rate per unit volume. Hence, the rate of nucleus formation per unit volume is given by

$$\dot{N} = \rho_K \dot{N}_{\Lambda},\tag{14}$$

where ρ_K is the Kuhn step density of the polymer.

A. Calculating Δf_i with finite extensibility

There remains to determine the values of Δf_i for each chain species under flow. From the RDP calculation, we have the structural conformation information for each species \mathbf{A}_i from which we can estimate Δf_i . This depends upon the degree of alignment at the Kuhn lengthscale, which is assumed to be proportional to the Kuhn segment nematic order, $P_{2,K,i}$. In the published polySTRAND model [34], the bond orientation for species i was calculated as

$$P_{2,K,i} = \frac{1}{N_e} \left(\Lambda_{i,\text{max}}^{(A)} - 1 \right),$$
 (15)

where $\Lambda_{i,\max}^{(A)}$ is the largest eigenvalue of the orientation tensor A_i and N_e is the number of Kuhn steps per entanglement. Then, $\Delta f_i = \Gamma P_{2,K,i}$ with $P_{2,K,i} = \Lambda_{\text{max}}/N_e$, where Γ is a constant of proportionality determined experimentally. However, using this method, $P_{2,K,i}$ can take values greater than one under strong flow, which is unphysical. The calculation is also inconsistent when finite extensibility becomes important. Consequently, we propose a modified method for calculating $P_{2,K,i}$ that corrects these issues, and the details of which are presented in the supplementary material. We reconsider the freely jointed chain calculation that leads to the force law for finite extensibility used in the Rolie-Double-Poly model and throughout the literature in polymer rheology [44,49]. Here, we follow similar reasoning to the calculation by Li and Larson [50], which was developed for measuring bond orientation in bead-spring simulations of dilute polymers.

The fundamental model, at the level of a tube segment, is a chain subsection of N_e freely jointed bonds each of fixed length l. We nondimensionalize the force f_i acting along the tube axis for chain species i as $X_i = f_i l/k_B T$. In the freely jointed chain model, this force is given by the inverse Langevin function, but here we use the Cohen approximation [44],

$$X_i = \frac{3\lambda_i}{\sqrt{N_e}} f_E(\lambda_i),\tag{16}$$

where $f_E(\lambda_i)$ is the finite extensibility function given in Eq. (2).

We then calculate $P_{2,K,i}$ for species i as a product of two terms, which are as follows: (i) the orientation order parameter of a freely jointed chain segment along the local tube axis, calculated in terms of X_i , and (ii) the orientation order parameter of tube segments relative to the direction of the largest principal component of A_i . As shown in the supplementary material, this gives

$$P_{2,K,i} = \frac{1}{2} \left(\frac{X_i^2 + 3 - 3X_i \coth X_i}{X_i^2} \right) \left(\frac{\Lambda_{i,\max}^{(A)}}{\lambda_i^2} - 1 \right), \quad (17)$$

with X_i obtained from Eq. (16). In the limit of strong orientation and strong stretching, $\Lambda_{i,\text{max}}^{(A)} \approx 3\lambda_i^2$ and X_i becomes large so that $P_{2,K,i}$ approaches a value of one, as required.

In the limit of small stretch, Eq. (17) reduces to

$$P_{2,K,i} = \frac{3}{10N_e} \left(\Lambda_{i,\text{max}}^{(A)} - \lambda_i^2 \right). \tag{18}$$

Comparing with Eq. (15), we see that the form is similar, but $\frac{0}{5}$ the numerical prefactor is smaller, so that when using Eq. (17), it becomes necessary to use a larger value of the proportionality constant Γ in $\Delta f_i = \Gamma P_{2,K,i}$ to obtain similar $\vec{\aleph}$ results as compared to the original polySTRAND formulation.

IV. SIMULATION OF FLOW-INDUCED **CRYSTALLIZATION**

To use the above models to simulate flow-induced crystallization in a complex flow, we developed an implementation of these equations using the rheoTool¹ toolbox within openFOAM [40].

A. Interpolation formula for the polySTRAND model

Although the polySTRAND model is significantly faster computationally than the original GO model simulations, it still requires several numerical steps to compute a free energy barrier toward nucleation. These are computationally costly to implement at each point in time and space in a large flow simulation. Therefore, we seek an efficient way to incorporate the polySTRAND calculation of the nucleaction rate within the simulations. We have found that the results of the polySTRAND model can be precomputed for a reasonable range of chain orientations and then embedded into openFOAM via an interpolation formula with a small number of parameters. This avoids solving the full polySTRAND model equations at each point in space and time, thus creating a much more efficient simulation.

We illustrate this methodology for our specific simulations. In Sec. II, we presented a rheological parameterization

for the HDB6 material, comprising four species of polymer chain calculated using the RDP model, plus one further species acting as unoriented solvent and for which, therefore, $\Delta f_0 = 0$. The volume fractions for these five species are given in the second column of Table I. We use the polySTRAND model to compute the effect of chain orientation, deduced from the RDP model, on flow-induced crystal nucleation rate.

Since at small values the enhancement of the nucleation rate is exponential in Δf_i , our proposed interpolation formula relates the natural logarithm of the normalized nucleation rate $\log(\dot{N}/\dot{N}_q)$, calculated from the polySTRAND model, to the free energy change per Kuhn segment, Δf_i , for each species i. The formula is a quotient function that comprises two polynomials in Δf_i for the numerator and the denominator. We found that quadratic order polynomials were sufficient to obtain a good fit to the polySTRAND results. The general structure of this interpolation formula is

$$\log\left(\frac{\dot{N}_{\Lambda}}{\dot{N}_{q}}\right) = \frac{\sum_{i} a_{i} \Delta f_{i} + \sum_{i} \sum_{j \leq i} b_{ij} \Delta f_{i} \Delta f_{j}}{1 + \sum_{i} c_{i} \Delta f_{i} + \sum_{i} \sum_{j \leq i} d_{ij} \Delta f_{i} \Delta f_{j}}.$$
 (19)

In keeping with the observed behavior of the polySTRAND model, this formula is linear in Δf_i for small orientations but approaches an asymptotic value for the nucleation rate at high orientations when the nucleation energy barrier is reduced to near zero.

The coefficients a_i , b_{ij} , c_i , and d_{ij} are fitting parameters that need to be adjusted for each specific material (i.e., they depend on the chemistry-dependent polySTRAND parameters, as well as on the specific volume fractions of the component species).

Now that we have the volume fractions of our chain species matched to rheological data, we can calculate the nucleation rate for various combinations of Δf_i . There are certain combinations of Δf_i that would not occur during our simulations, so we have reduced the range of the shorter fast relaxing species compared to the longer chain species. This allows our fitting procedure to be more accurate.

The range for Δf_4 was 0–0.8. Δf_3 and Δf_2 were 0–0.3. Δf_1 was 0–0.2. For each chain species, we used six data points, which gives 1296 overall data points with the different combinations of Δf_i taken into account. We perform a least squares fit to these data using the interpolation formulae, Eq. (19).

Sample results of fitting the nucleation rates obtained from the polySTRAND model to the above formula are shown in Fig. 4. These are shown for some specific values of Δf_1 , Δf_2 , and Δf_3 and for the full range of Δf_4 , though (as indicated above) the fitting was done for a wider set of values of Δf_i .

B. Logarithmic version of the Schneider rate equations

The polySTRAND model computes the rate of formation of nuclei from which crystals grow. We assume that, while flow accelerates nucleation, the polymer nevertheless crystallizes in a spherulitic structure. At higher flow strengths, shish-kebab structures are formed, but we assume that this limit is not reached. With these assumptions, the growth of

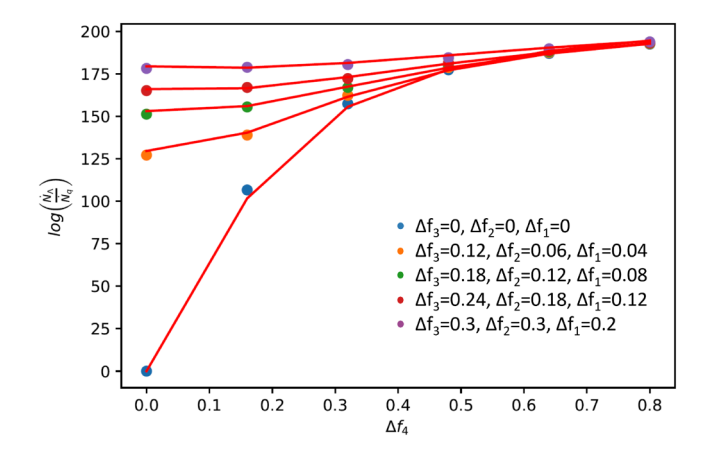


FIG. 4. Figure showing how Eq. (19) captures the enhancement of the nucleation rate as a function of Δf_{1-4} . The points show the values of $\log\left(\frac{\dot{N}_{\Delta}}{N_q}\right)$ calculated from the polySTRAND model and the lines show the results of fitting to Eq. (19). The nucleation rate results are shown for some specific values of Δf_1 , Δf_2 , and Δf_3 as a function of Δf_4 , although the fitting was done for a wider set of values of Δf_{1-3} . The figure shows the fit (progressing from bottom to top) when $\Delta f_1 = \Delta f_2 = \Delta f_3 = 0$; $\Delta f_1 = 0.04$, $\Delta f_2 = 0.06$, $\Delta f_3 = 0.12$; $\Delta f_1 = 0.08$, $\Delta f_2 = 0.12$, $\Delta f_3 = 0.18$; $\Delta f_1 = 0.12$, $\Delta f_2 = 0.18$, $\Delta f_3 = 0.24$; and $\Delta f_1 = 0.2$, $\Delta f_2 = \Delta f_3 = 0.3$.

isolated crystallites is described by Schneider rate equations [51]. These are given as follows:

$$\frac{DN}{Dt} = \dot{N},$$

$$\frac{DR}{Dt} = 2G_s N,$$

$$\frac{DS}{Dt} = 4\pi G_s R,$$

$$\frac{DV}{Dt} = G_s S,$$
(20)

where $\frac{D}{Dt}$ represents the material derivative. All quantities are per unit volume, V represents the volume of the crystalline phase, S is the total surface area of the crystallites, R is the total radius, and N is the number of nuclei. The quantities \dot{N} and G_s represent the nucleation rate per unit volume and the crystal growth rate, respectively.

Eq. (20) does not account for the impingement between neighboring crystals, which becomes significant as V approaches unity. Using the method of Avrami [52], we define the volume fraction of the crystal phase corrected for impingement as ξ_g , where

$$\xi_{g} = 1 - \exp(-V). \tag{21}$$

As the rate of nucleation depends exponentially on the values of Δf_i this can produce large spatial gradients in the local nucleation rate \dot{N} within the simulation. This occurs particularly at the wall of the contraction in contraction-expansion flow. This makes the numerical solution of the Schneider rate equations, Eq. (20), challenging due to the presence of the advection terms in the material derivative. This problem can be mitigated by instead computing with quantities related to logarithmic functions of variables associated with crystal growth. In order to form these functions, we need

TABLE III. Table showing the model parameters for the simulations at T = 125 °C. The growth rate and nucleation rates are for crystallization without flow.

Parameter	Value	Method
ρ_K	$3.04 \times 10^{21} \mathrm{cm}^{-3}$	Calculated using literature data [53], a findings from Matsuyama et al. [54], and Eq. (33)
ρ_a	$0.965 \mathrm{\ g\ cm^{-3}}$	Obtained from Matsuyama et al. [54]
M_e	$1600 \mathrm{g} \mathrm{mol}^{-1}$	Literature data and Eq. (35) [55]
$M_{ m mono}$	28 g mol^{-1}	Literature data ^a
C_{∞}	6.81	Literature data [53]
M_K	190.7 g mol^{-1}	Calculated using literature data [53] ^a
N_e	8.39	Calculated using literature data and Eq. (34) [53,55] ^a
$ au_e$	9 ns	Finding from Szanto et al. [56]
$ au_{ m O}$	0.127 ns	Calculated using literature data [53,55], a findings from Szanto et al. [56], and Eq. (36)
$ ho_c$	1 g cm^{-3}	Finding from Martin et al. [57]
r_l	$1.49 \times 10^{-6} \text{ cm}$	Finding from Zhou et al. [58]
M_{n^*}	$5.35 \times 10^6 \mathrm{g mol}^{-1}$	Calculated using the findings from Martin et al. [57] and Zhou et al. [58]
n^*	43 400	Obtained by fitting ϵ_B and μ_S in the polySTRAND model to the form of the nucleation barrier reported by Yi et al. [59] and
		to literature data [53,57,58] ^a
G_s	$0.3 \mu \mathrm{m \ s}^{-1}$	Obtained from Hoffman et al. [60]
\dot{N}_q	$4.76 \times 10^{-80} \mathrm{s}^{-1}$	Obtained from fitting ϵ_B and μ_S in the polySTRAND model to the nucleation barrier found by Yi et al. [59]
$\dot{N}_{ m het}$	$1 \times 10^{-2} \mathrm{cm}^{-3} \mathrm{s}^{-1}$	Chosen to provide a floor rate of crystal nucleation in the melt, see Sec. IV B.
Γ_0 , Γ_{FE}	2, 10/3	Γ_0 value suggested by Anwar and Graham [20] from molecular dynamics simulations of a bimodal polyethylene blend.
		Here, Γ_{FE} is the value adjusted to take account of the numerical factor of 10/3 arising from the change in the calculation of
		$P_{2,K}$ with finite extensibility.

^aCarnegie Mellon University, Sample molecular weight calculation (2023), https://www.cmu.edu/gelfand/lgc-educational-media/polymers/what-is-polymer/molecular-weight-calculation.html (accessed January 23, 2023).

to define an appropriate scale for each of the quantities under consideration.

Although, in principle, using the quiescent nucleation rate for the scales for each quantity in the Schneider rate equations is the logical choice, the quiescent nucleation rate, $\rho_K \dot{N}_q$, in our example is of order $10^{-59}\,\mathrm{cm}^{-3}\,\mathrm{s}^{-1}$. This vanishingly small rate is far too small to provide a sensible scaling. In practice, this means that the energy barrier to nucleation is such that any nucleation events under quiescent conditions will be from heterogeneous rather than homogeneous nucleation. We can, therefore, add an additional rate of nucleation $\dot{N}_{\rm het}$ to represent the heterogeneous nucleation rate per unit volume. Provided that the value of $\dot{N}_{\rm het}$ is sufficiently low that it does not lead to the growth of a significant number of crystallites on the time scale of the simulations, its value does not affect the flow-induced acceleration. In the following calculations, we include a heterogeneous nucleation rate of $\dot{N}_{\rm het} = 1 \times 10^{-2} \, {\rm cm}^{-3} \, {\rm s}^{-1}$, which is sufficiently small to not produce significant crystallization but is much larger than the quiescent homogeneous nucleation rate. With the inclusion of this heterogeneous nucleation rate, Eq. (20) becomes

$$\frac{DN}{Dt} = \dot{N} + \dot{N}_{\text{het}}.$$
 (22)

The inclusion of \dot{N}_{het} , therefore, provides a floor for the nucleation rate in regions where \dot{N} is effectively zero. In such regions, the expected number density of crystal nuclei formed is given by

$$N_c = \dot{N}_{\text{het}} t_{\text{char}},\tag{23}$$

where t_{char} is a characteristic simulation time.

Using N_c , we can define a new dynamical variable

$$u_N = \log\left(1 + \frac{N}{N_c}\right),\tag{24}$$

such that

$$N = N_c(e^{u_N} - 1). (25)$$

Substituting this into the first of the Schneider rate equations, we obtain an evolution equation for u_N in the form

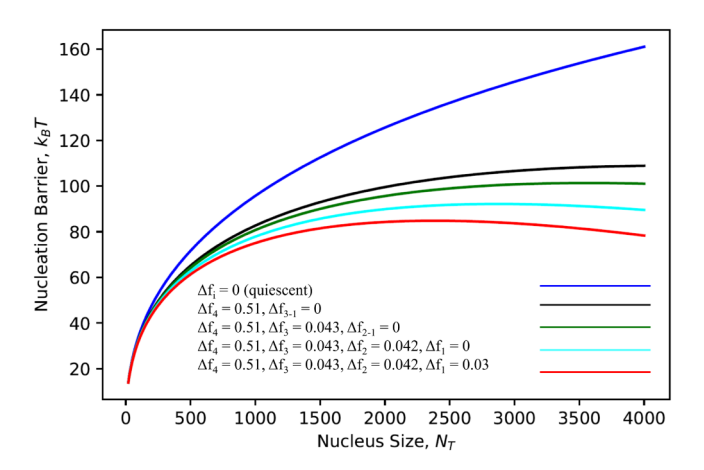


FIG. 5. Graph of nucleation barrier as a function of nucleus size N_T (in units of number of Kuhn segments) as predicted by the polySTRAND model. This shows how each of the different chain species in the polymer melt reduces the nucleation barrier. Each chain species contributes in a non-trivial way, highlighting the importance of taking all the species into account in our calculations of the nucleation barrier. This figure shows the results, from top to bottom, for $\Delta f_1 = 0$, $\Delta f_{1-3} = 0$, $\Delta f_4 = 0.51$, $\Delta f_{1-2} = 0$, $\Delta f_3 = 0.043$, $\Delta f_4 = 0.51$; $\Delta f_1 = 0$, $\Delta f_2 = 0.042$, $\Delta f_3 = 0.043$, $\Delta f_4 = 0.51$; and $\Delta f_1 = 0.03$, $\Delta f_2 = 0.042$, $\Delta f_3 = 0.043$, $\Delta f_4 = 0.51$.

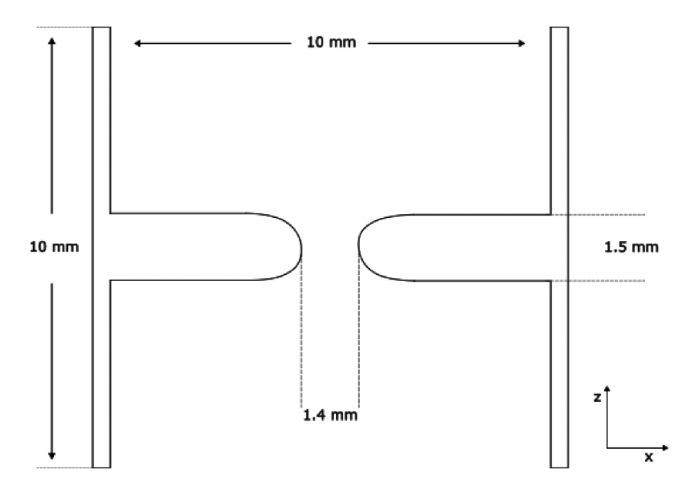


FIG. 6. This image shows the dimensions for our computational domain. Inspiration taken from Ref. 41.

$$\frac{Du_N}{Dt} = \frac{\dot{N} + \dot{N}_{\text{het}}}{N_c e^{u_N}}.$$
 (26)

The subsequent Schneider rate equations can be treated in a similar way.

For R, we define a typical scale as $R_c = \dot{N}_{het}G_s t_{char}^2$ and

$$u_R = \log\left(1 + \frac{R}{R_c}\right),\tag{27}$$

where

$$\frac{Du_R}{Dt} = \frac{2G_sN}{R_c e^{u_R}}. (28)$$

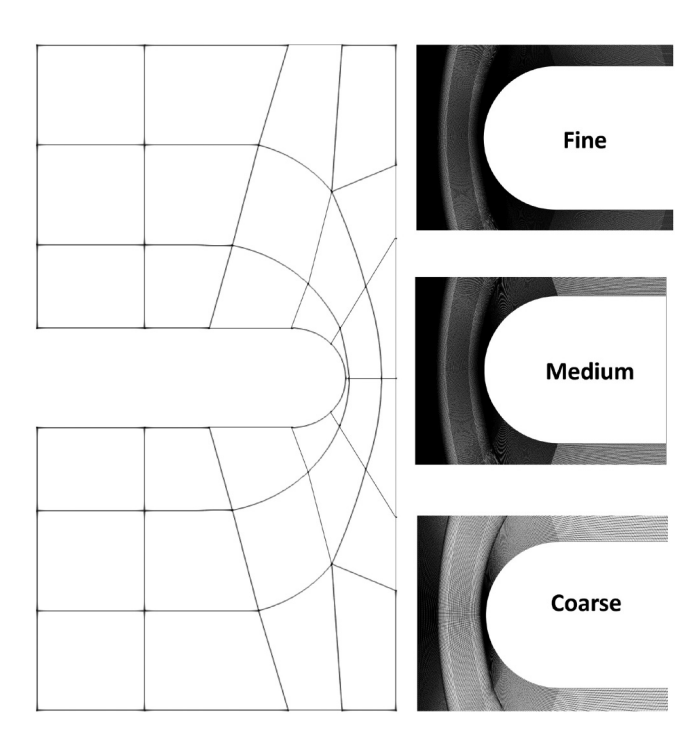


FIG. 7. This figure shows the mesh block structure and the zoomed in view of the contraction region for different mesh resolutions.

TABLE IV. Table showing the different mesh statistics for the coarse, medium, and fine meshes.

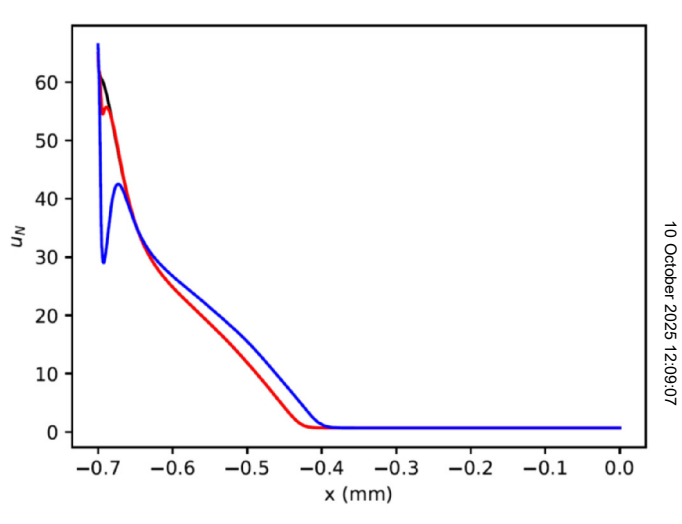
	Coarse mesh	Medium mesh	Fine mesh
Points	346 562	1 381 122	1 941 402
Cells	172 000	688 000	968 000
Faces	689 280	2 754 560	3 874 700
Internal faces	342 720	1 373 440	1 933 300

Similarly, for S, we define $S_c = \dot{N}_{het} G_s^2 t_{char}^3$, such that

$$u_S = \log\left(1 + \frac{S}{S_c}\right),\tag{29}$$

satisfying

$$\frac{Du_S}{Dt} = \frac{4\pi G_s R}{S_c e^{u_S}}. (30)$$



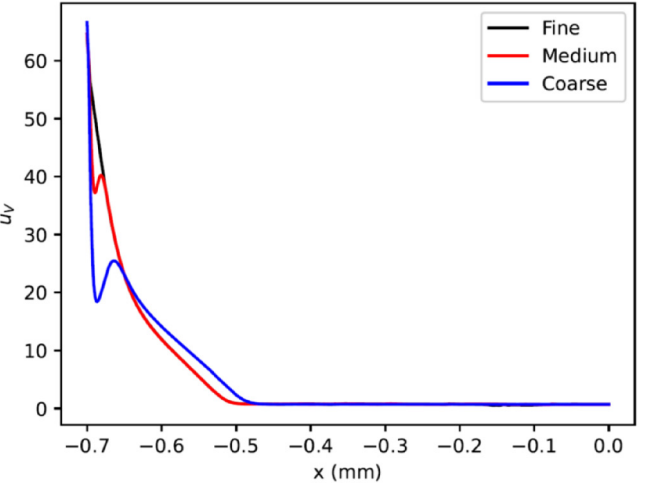


FIG. 8. Line plots showing how the logarithmic measures of crystal number and volume fraction, u_N and u_V , respectively, vary across the narrow part of the contraction as a function of distance from the symmetry line, for $Q = 1.68 \,\mathrm{mm^2\,s^{-1}}$ and $t = 10 \,\mathrm{s}$. Both quantities have a maximum at the wall and decrease toward the center line with convergence with mesh refinement seen for both functions. The *x*-axis represents the distance from the symmetry line set at 0. Both plots show the results, from top to bottom, for the fine, medium, and coarse mesh.

TABLE V. Table showing the different flow rates used in the simulations along with the corresponding pressure drop.

$Q(\text{mm}^2\text{s}^{-1})$	ΔP (MPa)
1.26	9
1.68	10.5
2.19	12
2.62	13.5

Finally, for V, we define $V_c = \dot{N}_{het} G_s^3 t_{char}^4$ with

$$u_V = \log\left(1 + \frac{V}{V_c}\right) \tag{31}$$

so that

$$\frac{Du_V}{Dt} = \frac{G_s S_{\text{tot}}}{V_c e^{u_V}}.$$
 (32)

C. Crystallization model parameters

The polySTRAND flow-induced crystallization model requires a number of parameters, which are known to varying

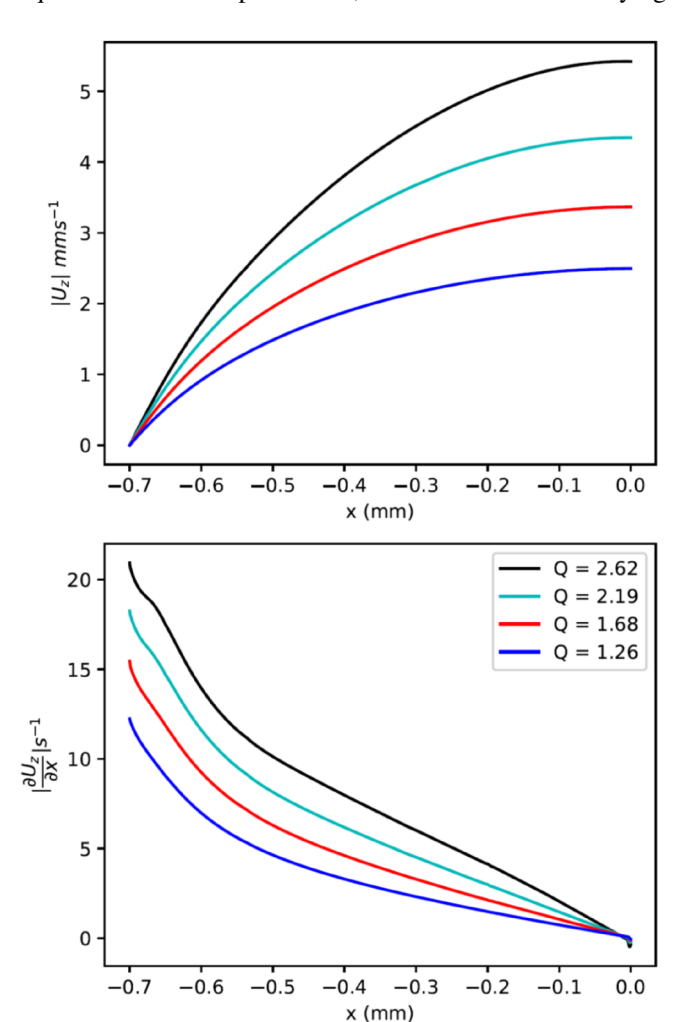


FIG. 9. Line plots showing the magnitude of the *z*-component of the velocity along with its gradient in the *x*-direction across the narrow part of the constriction for the four different flow rates investigated at $t = 10 \, \text{s}$. The *x*-axis represents the distance from symmetry line along the center of the contraction. In both figures, the lines show the results, from top to bottom, for Q = 2.62, Q = 2.19, Q = 1.68, and Q = 1.26.

degrees of certainty [34]. We consider the parameters in the model relevant to the case of polyethylene at 125 °C, as used in the experiments of Scelsi *et al.* [41].

The density of Kuhn segments is given by

$$\rho_K = \frac{\rho_a N_A}{M_K},\tag{33}$$

where ρ_a is the amorphous density of the polymer, N_A is the Avogadro number, and M_K is the Kuhn molecular weight found from $M_K = M_{\text{mono}} C_{\infty}$, where M_{mono} is the monomer molecular weight and C_{∞} is the characteristic ratio.

The number of steps per entanglement segment is given by

$$N_e = \frac{M_e}{M_K},\tag{34}$$

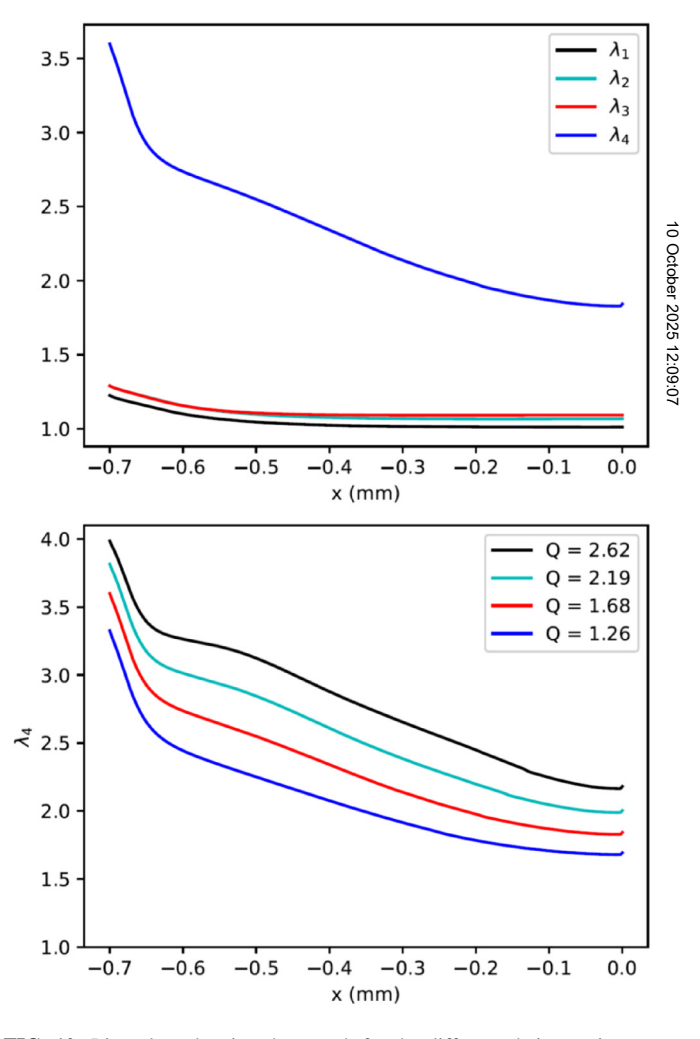


FIG. 10. Line plots showing the stretch for the different chain species at a flow rate of $Q=1.68\,\mathrm{mm^2\,s^{-1}}$ and also the values of λ_4 for the different flow rates at $t=10\,\mathrm{s}$. The line plots show the change in these variables from the wall of the contraction region to the center of the channel across the center of the contraction. The *x*-axis represents the distance from the center of the contraction. The top figure shows the results, from top to bottom, for λ_4 , λ_3 , λ_2 , and λ_1 . The bottom figure shows the results, from top to bottom, for Q=2.62, Q=2.19, Q=1.68, and Q=1.26.

where M_e is the entanglement molecular weight calculated via

$$M_e = \frac{\rho_a RT}{G_N^0},\tag{35}$$

where R is the real gas constant, T is temperature, and G_N^0 is the plateau modulus.

We also need to obtain parameters governing the quiescent nucleation kinetics so that we can predict FIC using the polySTRAND model. The monomer attachment time, τ_0 , is given by projecting the entanglement time τ_e down to the Kuhn step length scale,

$$\tau_0 \approx \tau_K = \frac{\tau_e}{N_e^2}.\tag{36}$$

The form of the quiescent nucleation barrier is found from the quiescent free energy of crystallization per monomer, ϵ_B , and the surface energy cost, μ_S , which are chosen to match the literature data for the quiescent nucleation rate, \dot{N}_q , and critical nucleus size, n^* . The latter can be estimated via

$$n^* = \frac{M_{n^*}}{M_K},\tag{37}$$

where the mass of the critical nucleus (assumed to be spherical) is $M_{n^*} = 4\pi \rho_c N_\Lambda r_l^3/3$, for lamella thickness $2r_l$ and crystal density ρ_c . Values for n^* and \dot{N}_q were available in the literature, and these can then be matched in the model by

adjusting the parameters ϵ_B and μ_S given the known value for τ_0 .

Estimates for the spherulitic growth rate, G_s , can be obtained from the literature. Likewise, values for the prefactor Γ that relates Δf to $P_{2,k}$ are suggested in the literature [20,34]. Note there is a need to distinguish between Γ_0 for the original model and Γ_{FE} when finite extensibility is included as discussed in Sec. III A above. There is some debate over the choice of Γ , and further details are given in Sec. V C.

Table III gives a summary of the parameter values used and the methods and references used to determine them.

We now examine how the effect of flow changes the energy barrier to nucleation. The nucleation rate is related to the nucleation barrier via an exponential function. Therefore, flow can have a dramatic effect on the nucleation rate. In a polydisperse melt, each chain species needs to be taken into account to get an accurate prediction of the nucleation barrier.

Figure 5 shows how each of the different chain species in our polymer melt contributes to the reduction in the energy barrier. The values chosen for Δf_i in Fig. 5 are the maximum values for Δf_i obtained from a simulation in Sec. VB (Fig. 13). This illustrates how flow dramatically reduces the nucleation barrier within the melt in our simulations.

Figure 5 shows that the barrier to nucleation decreases by multiple order of k_BT due to the flow. The critical nucleus size also decreases by a factor of 20 to roughly 1500 monomers. A large proportion of this reduction is due to the glongest chain species, and the rest is a result of the remaining

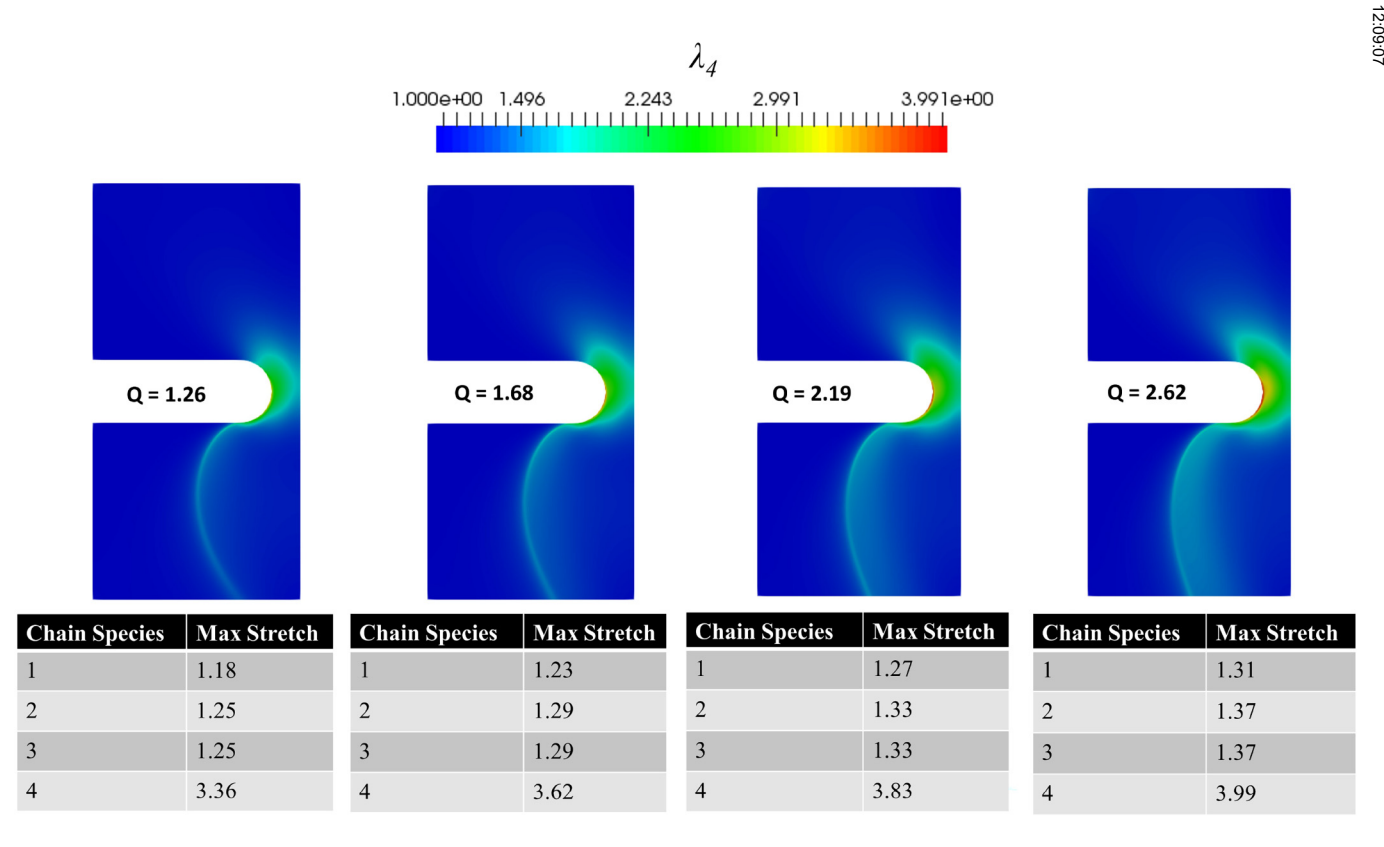


FIG. 11. This figure shows how the λ_4 parameter changes due to the flow rate of the different simulations at t = 10 s. As expected, most of the activity is in the contracting region. The tables underneath the contour plots show the maximum value for λ_i for the rest of the chain species in the different simulation runs.

three smaller chain species. Although the contribution of the smaller, fast relaxing, chain species may appear insignificant when compared to the long-chain species, these small chain species make up a larger volume fraction of the melt so do contribute to the reduction of the energy barrier in a nontrivial way.

D. Contraction geometry

For our investigation, we chose to look at the effects of a contraction expansion geometry based on the experimental study conducted by Scelsi *et al.* [41]. The dimensions used for the geometry are shown in Fig. 6. The mesh is oriented such that in a Cartesian coordinate system, the *z*-axis represents the vertical direction and the *x*-axis is the horizontal direction.

Since the geometry is symmetric about the center line, only half of the contraction geometry needs to be calculated. The fluid flow is developed by imposing a non-zero pressure difference between the inlet and the outlet with no-slip boundary conditions applied at the walls, with linear extrapolation used for the boundary conditions for the conformation tensors at the wall.

Figure 7 shows the overall block structure of the mesh along with a view of the contraction region for three different mesh resolutions. The summary statistics for each mesh are given in Table IV.

The variables that are most sensitive to mesh resolution are from the Schneider rate equations. The line plots in Fig. 8 show how logarithmic measures of crystal number and volume fraction u_N and u_V develop across the center of the contraction from the wall to the symmetry-line of the contraction for different meshes. There is convergence of our solutions for both quantities in the contraction region as the mesh resolution increases.

V. RESULTS

In this section, we discuss the results from a set of simulations in which the rheology model detailed in Sec. 1 is combined with the flow-induced crystallization implementation detailed in Sec. 2, for prediction of crystallization under flow. We first consider the flow dynamics and then how this affects the crystallization dynamics. We compare our results qualitatively with those of Scelsi *et al.* [41].

The flow is driven by imposing a nonzero pressure difference between the inlet and the outlet. Table V shows the four different values used for the pressure drop and the corresponding area flow rate since the simulation is two-dimensional.

A. Polymer flow configuration

Figure 9 shows the magnitude of the z-component of the velocity and its gradient in the x-direction across the narrow part of the contraction. The latter is the dominant contribution to the shear rate in the contraction region. The results are shown for four different flow rates at the end of the simulation (t = 10 s) where the flow has reached steady state; however, the crystallization kinetics are continuously

developing. As expected, the highest shear rates are found at the wall of the contraction region decreasing to zero at the center line of the geometry.

We next examine the stretch, $\lambda_i = 1/3\sqrt{\text{Tr}\mathbf{A}_i}$, of each species within the blend. The upper plot in Fig. 10 shows the stretch, λ_i , of the different chain species at flow rate $Q = 1.68 \, \text{mm}^2 \, \text{s}^{-1}$ at $t = 10 \, \text{s}$ across the contraction. From Fig. 9, we can observe that the wall shear-rate is around $15 \, \text{s}^{-1}$, which is sufficient to produce significant extension of the slowest chain species, since $\tau_{s,4} = 0.5 \, \text{s}$, but not of the three faster modes. The lower plot in Fig. 10 shows how the stretch of the slowest chain species, λ_4 , varies with the flow rate. In all cases, we can see that the stretch is largest at the wall for all chain species and decreases toward the center line. However, λ_4 does not decrease to unity on the center line, demonstrating that there is stretch of this chain species due to the extensional deformation induced by the contraction. Nevertheless, the largest contributing factor to the

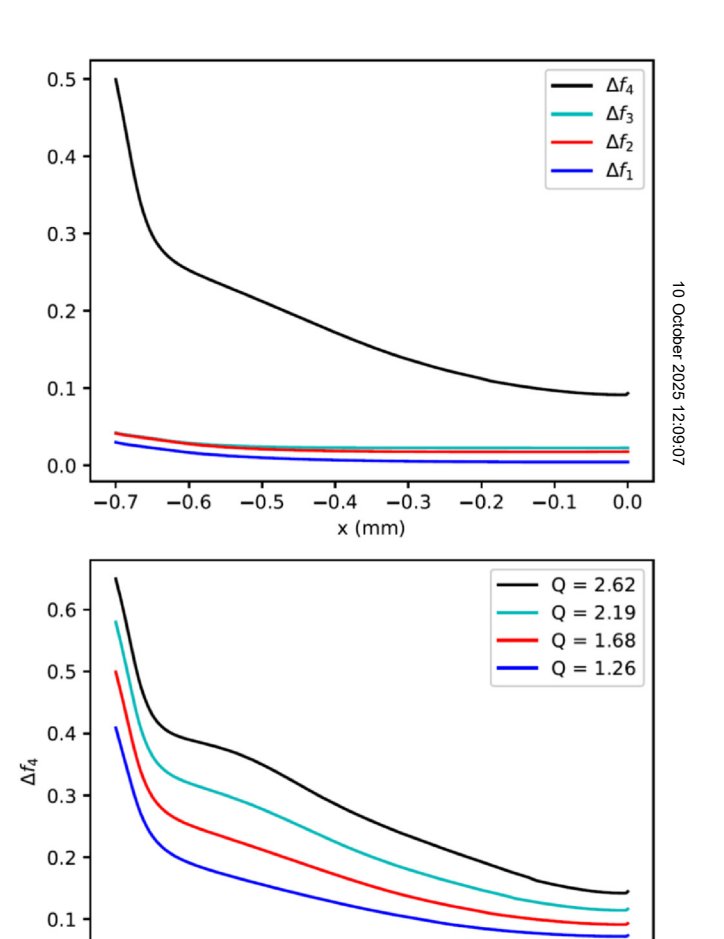


FIG. 12. The top line plot shows how Δf_i develops across the contraction when $Q = 1.68 \,\mathrm{mm^2\,s^{-1}}$ and $t = 10 \,\mathrm{s}$. The bottom line plot shows how Δf_4 develops across the contraction for the four different flow rates investigated at $t = 10 \,\mathrm{s}$. The line plots show the change in these variables from the wall of the contraction region to the center of the channel in the middle of the mesh. The *x*-axis represents the distance from the center of the mesh, where the center is set at 0. The upper plot shows the results, from top to bottom, for Δf_4 , Δf_3 , Δf_2 , and Δf_1 . The lower plot shows the results, from top to bottom, for Q = 2.62, Q = 2.19, Q = 1.68, and Q = 1.26.

-0.3

x (mm)

-0.2

-0.1

0.0

-0.6

-0.5

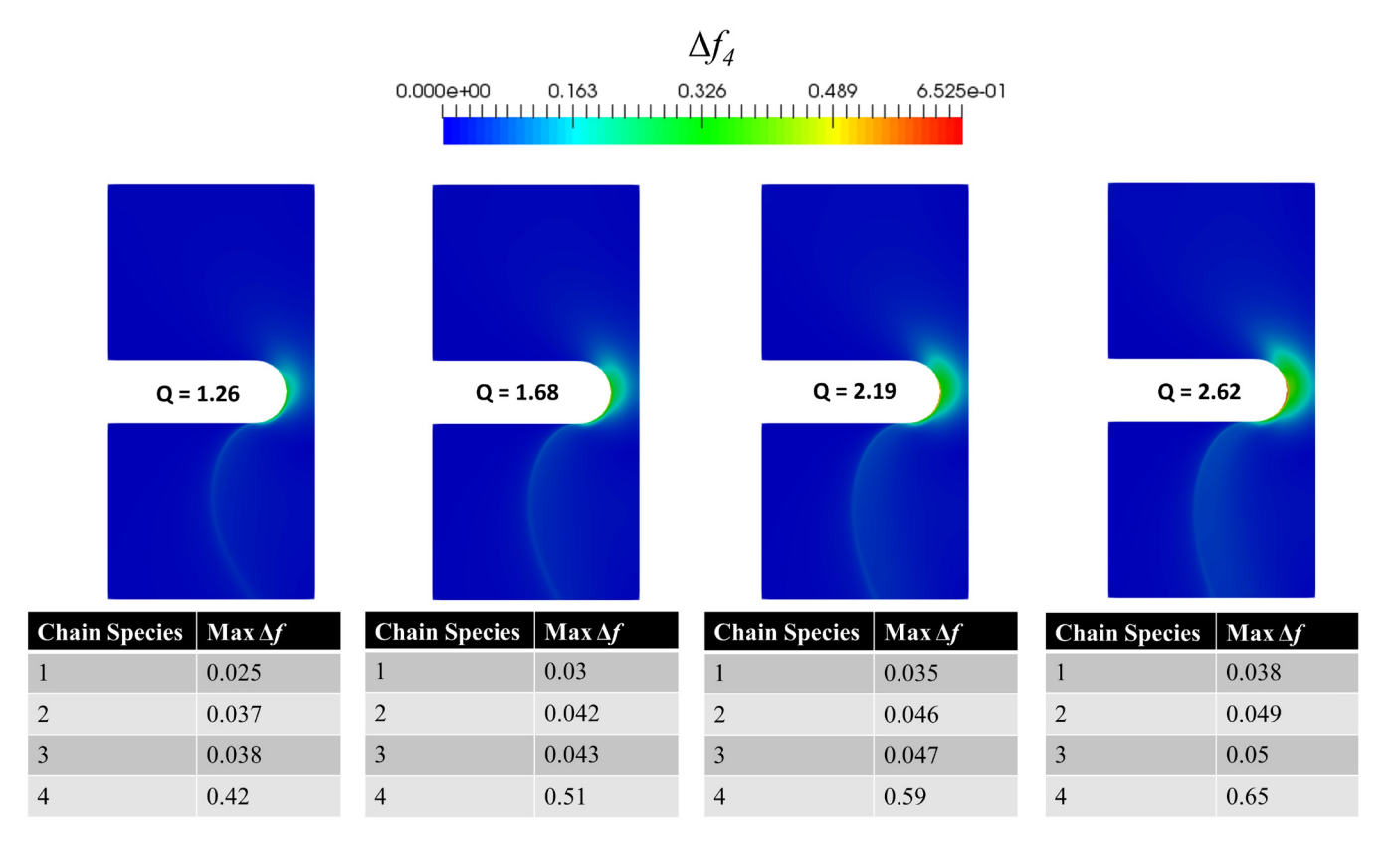


FIG. 13. This figure shows how the contraction affects the Δf_4 parameter at the end of the simulations for the different flow rates at t = 10 s. The tables underneath give the maximum value for Δf_i for the rest of the chain species in each simulation.

stretch is the shear rate at the wall, rather than the extension rate along the center line.

Figure 11 provides contour plots of λ_4 for the entire simulation domain after a time of 10 s for each of the flow rates. Although the largest values occur near the wall at the center of the contraction, where the largest shear rates occur, advection by the flow leads to the formation of a "fang" of stretched material downstream corresponding to the birefringence structures report by Lee *et al.* [61]. This suggests that the majority of the crystal nucleation will occur at the wall of the contraction region with crystals advecting from this region. We also observe a broader region of stretch within the contraction due to the extensional flow. As noted above, the strain rates are not sufficient to induce large stretching of the other chain species, whose maximal values are given in the tables underneath each picture.

B. Crystallization dynamics

Having determined the polymer conformation from solving the flow for the RDP model, we can now proceed to calculate how this changes the rate of nucleation. The upper plot in Fig. 12 shows the free energy change per Kuhn segment, Δf_i , across the center of the contraction for each of the chain species when Q = 1.68 mm² s⁻¹ and t = 10 s. As might be expected, these results mirror the corresponding values for λ_i of the different chain species shown in Fig. 10 with the largest values of Δf_i found at the wall and decreasing toward the center line. It is important to note that although the change in free energy corresponding to the longest chain

species, Δf_4 , is largest, $\Delta f_i \neq 0$ for all four chain species. As a consequence, all chain species contribute to the reduction of the nucleation barrier as shown in Fig. 5. The lower plot in Fig. 12 shows how Δf_4 develops across the contraction for the four different flow rates investigated.

Figure 13 provides an equivalent contour plot to Fig. 11 for the values of Δf_4 at t = 10 s. The tables beneath each picture show the maximum value of Δf_i for the remaining

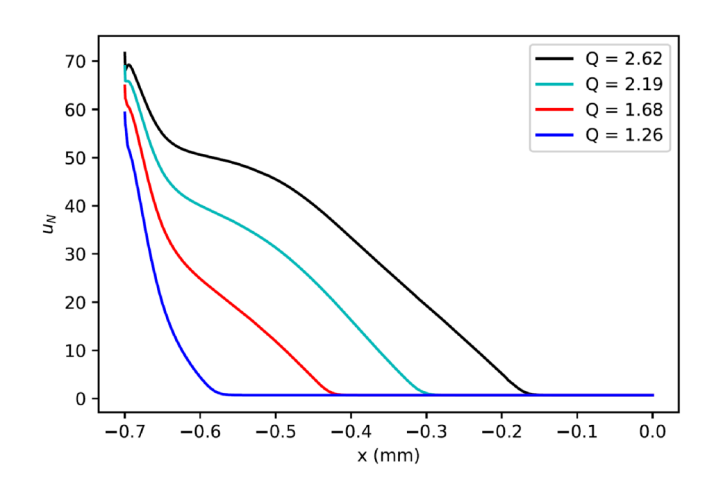


FIG. 14. Line plot that shows the comparison of the u_N parameter for the different flow rates at t = 10 s. This line plot shows the change in u_N from the wall of the contraction region to the center of the channel in the middle of the mesh. The *x*-axis represents the distance from the center of the mesh, where the center is set at 0. The lines show the results, from top to bottom, for Q = 2.62, Q = 2.19, Q = 1.68, and Q = 1.26.

10 October 2025 12:09

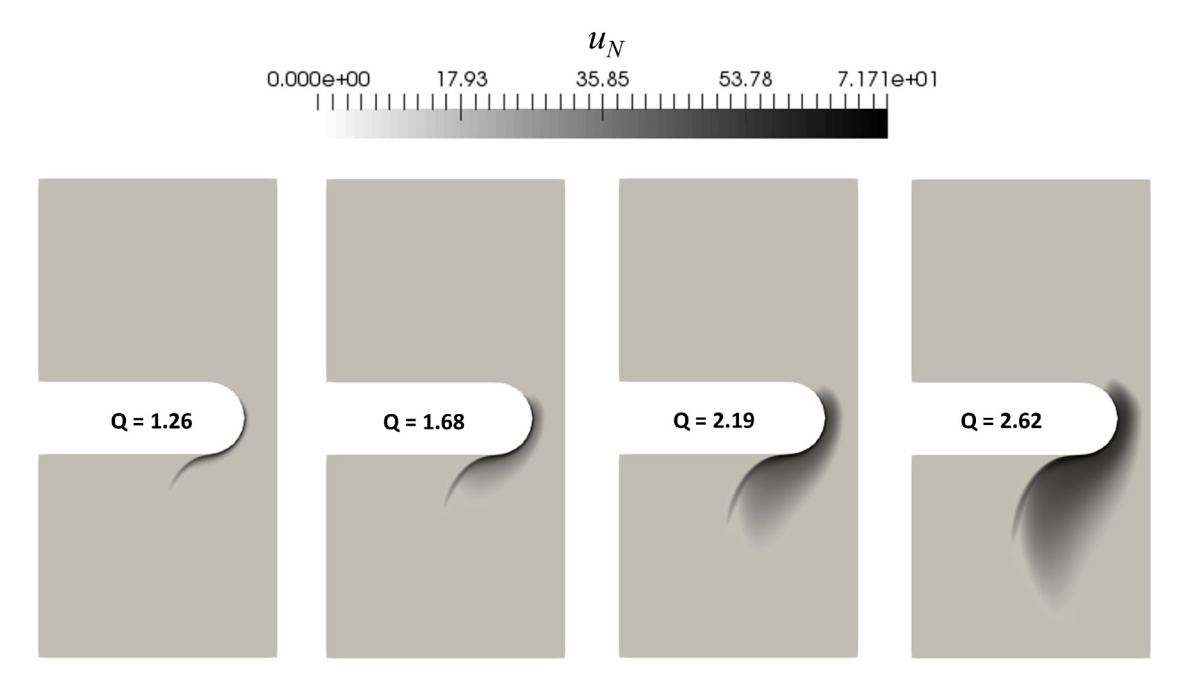


FIG. 15. This figure shows how the development of u_N changes for the different flow rates at t = 10 s.

chain species. The spatial distribution of Δf_4 mirrors that found for the chain stretch, with the highest values occurring at the wall of the contraction region owing to the strong shearing forces present in this region. Δf_4 is largely being unaffected before the contraction. It is important to note that the nucleation rate increases exponentially with the change in free energy. Hence, we expect that all accelerated crystal nucleation will originate in the contraction and be advected from there, with crystal growth occurring downstream.

Figure 14 shows how $u_N = \log(1 + N/N_c)$, which measures the number density of crystal nuclei, varies across the center of the contraction from the wall to the symmetry line at t = 10 s. The largest values of u_N are found at the wall of the contraction due to the large values of Δf_i . u_N decreases toward zero away from the wall. Although the values of Δf_i remain above zero away from the wall, this is insufficient to provide a significant increase in the rate of nucleation when compared with the heterogeneous background rate and when compared to the time taken for the polymers to advect through this region. Close to the wall, not only is the nucleation rate higher, but the no-slip boundary condition means that the polymers have a longer residence time in this region, giving greater time for nuclei to develop.

Figure 15 shows the distribution of u_N throughout the flow domain after $t = 10 \,\mathrm{s}$. At low flow rates, crystal nucleation is confined to the narrow region of fluid that has been advected from the wall of the contraction where the strong shear results in an increase in the nucleation rate, N. This characteristic "fang" shape forms along a streamline of the flow and is seen in the experiments of Scelsi et al. [41]. This "fang" lengthens and becomes more prominent as the flow rate increases since the increased flow increases the distance travelled by the polymers from the onset of the flow. There is also a broadening of the crystal nucleation region further into the bulk flow as flow rate increases. This can be attributed to the higher extension rate at the higher flow rate, meaning that extension contributes more to the deformation of polymer chains at the higher flow rates, hence leading to more nucleation further away from the wall in the bulk.

We next examine u_V , the logarithm of the volume fraction $\frac{Q}{R}$ before correction for impingement. Figure 16 shows the development of u_V from the wall of the contraction to the $\frac{8}{8}$ center of the mesh at t = 10 s. Compared to the corresponding figure for u_N , Fig. 14, the large values are more closely $\stackrel{\circ}{\approx}$ confined to the region near the wall. This is because, in addition the number of nuclei being larger, the fluid velocity is slower giving a longer residence time for the crystals to grow before being advected downstream. Figure 17 compares the distribution of u_V at t = 10 s. The spatial distribution of u_V is

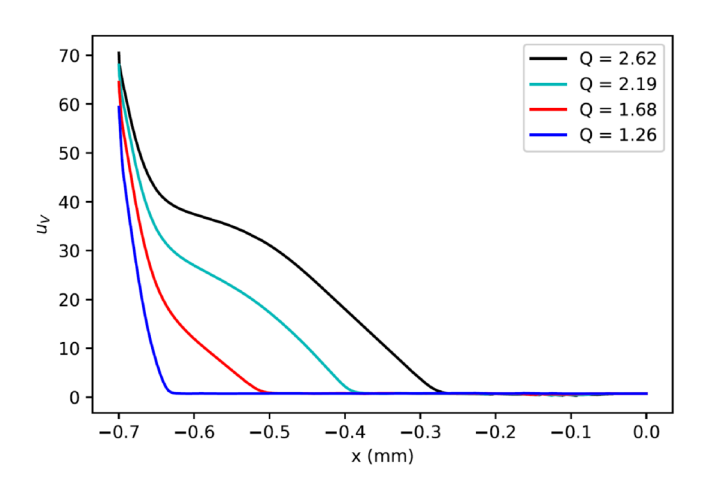


FIG. 16. Line plot that shows the comparison of the u_V parameter for different speed simulations at t = 10 s. The line plot shows the change in u_V from the wall of the contraction region to the center of the channel in the middle of the mesh. The x-axis represents the distance from the center of the mesh, where the center is set at 0. The lines shows the results, from top to bottom, for Q = 2.62, Q = 2.19, Q = 1.68, and Q = 1.26.

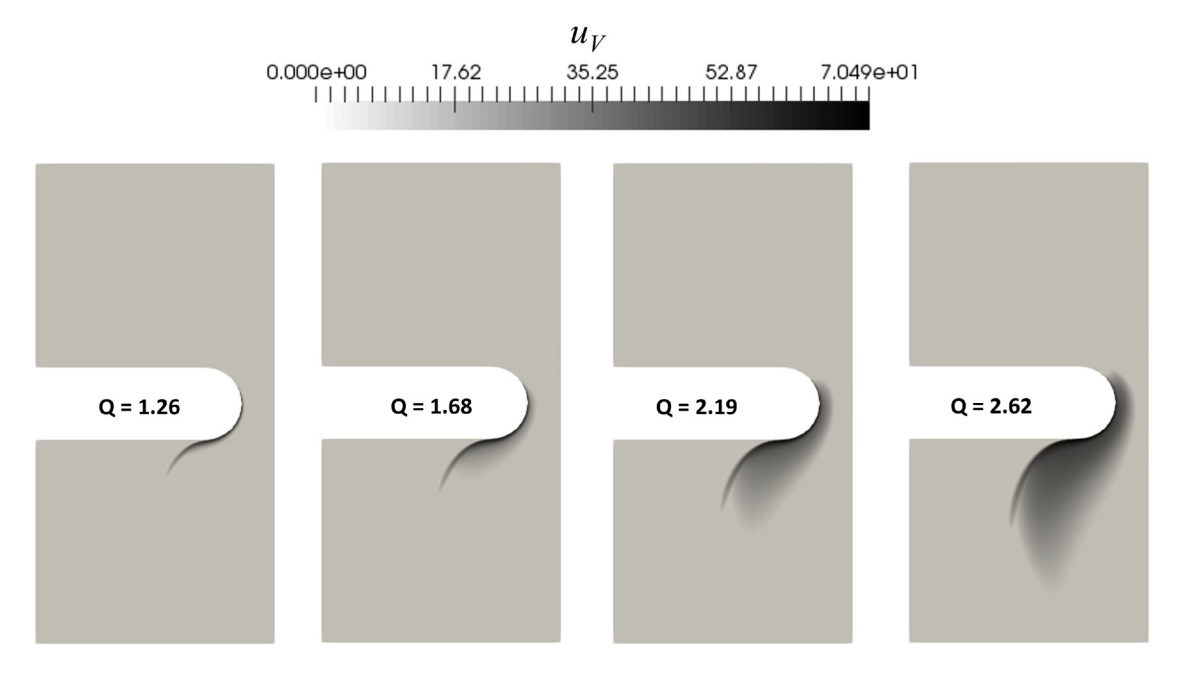


FIG. 17. This figure shows how u_V changes when the flow rate is changed in each of the four different cases investigated at t = 10 s.

almost identical to that of u_N , with highest level of crystal development occurring at the wall of the contraction with advected crystals continuing to grow as they are advected downstream. The characteristic "fang" shape is again present and becomes more defined with increasing flow rate.

This then gives us the platform to look at the results of the experimentally measured volume fraction, ξ_G , that is corrected for impingement of crystals. Figure 18 compares the distributions of ξ_G at $t=10\,\mathrm{s}$. This shows that true volume fraction of crystals as would be observed experimentally, unlike u_V that is on a logarithmic scale. The observable crystallization is confined to the "fang" of material that has been advected downstream from the wall of the contraction.

The "fang" structure becomes more defined with increasing flow rate and also grows in length. The latter is partly a consequence of comparing the results at a fixed flow time (rather than at fixed volumetric flow) so that at higher flow rates the crystals get advected further down stream. This localization of crystallization to the "fang" is precisely where crystallization is found experimentally [41]. However, we observe crystallization at lower flow rates than observed in experiment. There are a number of potential reasons for this discrepancy. First, as noted in Sec. II A, the RDP model does not strictly apply to the polyethylene melt used in the experiments, which contains some long-chain branches. In particular, the choice of stretch relaxation times does not capture that

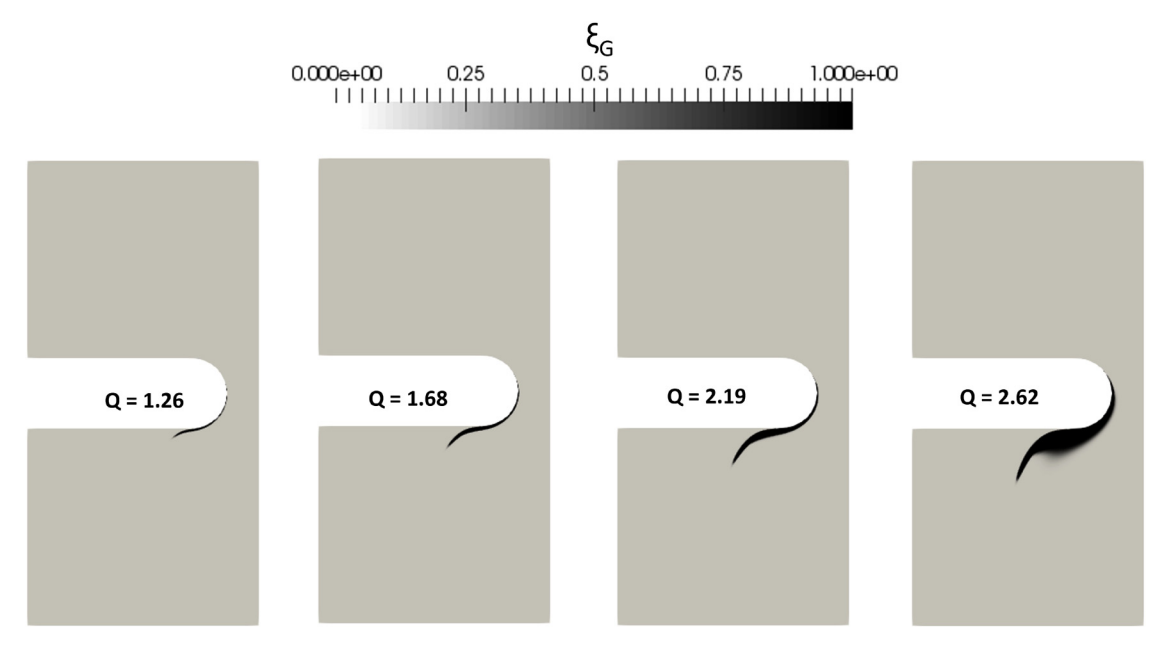


FIG. 18. This figure shows how ξ_G develops for the different flow rates at $t=10\,\mathrm{s}$.

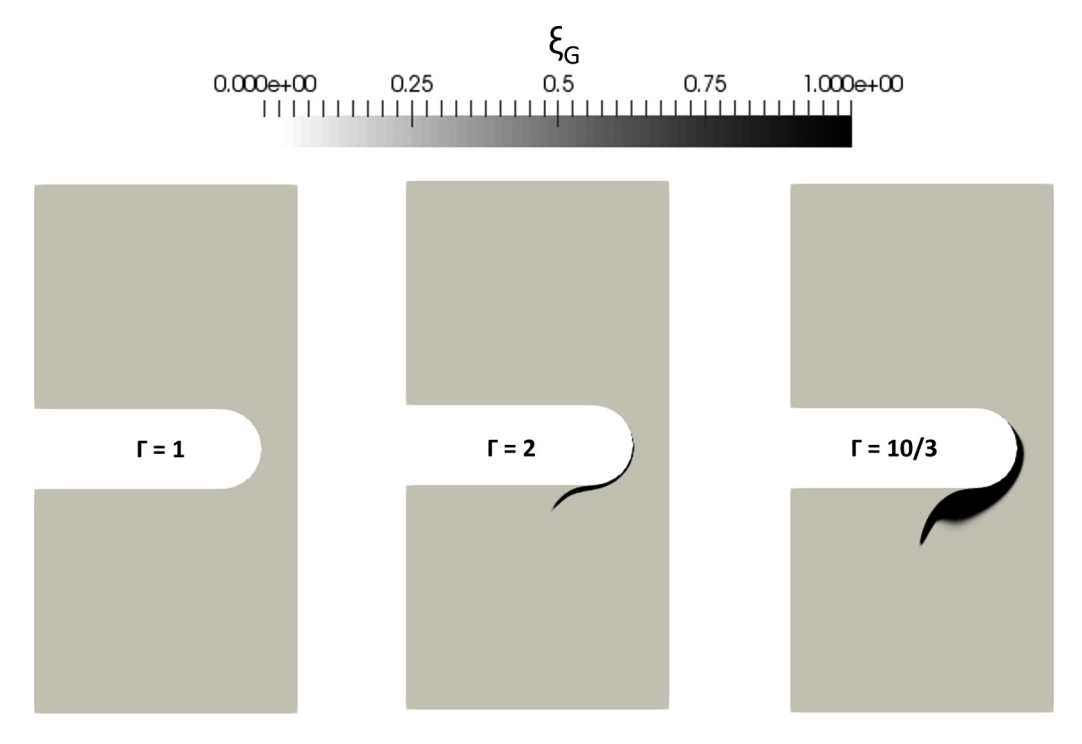


FIG. 19. This figure shows how variation in Γ affects the profile of ξ_G when Q = 1.68.

transient extensional viscosity over the range of extension rates. Smaller values of $\tau_{s,i}$ would shift the onset of flow-induced crystallization to higher flow rates, but the spatial distribution would remain the same. There are also several parameters in the polySTRAND model, whose values are only known approximately, but which affect the magnitude of flow-induced nucleation. Notably among these, Γ is the constant of proportionality that relates the Kuhn segment nematic order parameter, $P_{2,K,i}$, to the crystallization free energy change per Kuhn segment, Δf_i .

C. Variation of the Γ parameter

In the polySTRAND model, the free energy of attachment of each chain species Δf_i is assumed to be proportional to the Kuhn segment nematic order parameter $P_{2,K,i}$ with constant of proportionality Γ . In the original polySTRAND paper supplementary material [34], it is suggested that Γ should be of order 1 with its value chosen to fit to experimental measurements on FIC. A value of $\Gamma = 0.65$ is suggested for polyethylene based on MD simulations that provide a direct calculation of $P_{2,K,i}$. However, as these MD simulations combined the carbon and hydrogen atoms for computational efficiency, this may give rise to a discrepancy between these results compared to experimental results for polyethylene. We also note that our new method of calculating $P_{2,K,i}$, given in Sec. III A, results in a factor of 3/10 in the small stretch limit given by Eq. (18), as compared to the original polySTRAND model [34]. This suggests that Γ , using our new calculation, should be a factor of 10/3 larger than the value of Γ from the original polySTRAND model. To account for this increase, we chose a value of $\Gamma = 2$ for our simulations presented above. However, given the uncertainty in this estimate we now consider how changes to Γ affect the prediction of crystallisation.

The prediction for the crystal volume fraction ξ_G for three different values of $\Gamma=1,2,10/3$ are shown in Fig. 19. Since Γ is the constant of proportionality between Δf_i and $P_{2,K,i}$, increasing Γ produces an exponential increase in the orate of flow induced nucleation. As a consequence, predictions of the degree of FIC, but not its location, are very sensitive to the value of this parameter. In particular, it can be seen that if Γ is reduced to unity we no longer observe crystal formation at this flow rate. This may partially explain why our simulations with $\Gamma=2$ predict the onset of FIC at lower flow rates than found in experiment.

VI. CONCLUSION

The aim of this paper was to demonstrate that it is possible to use molecularly informed coarse-grained models to predict flow-induced nucleation within a complex flow geometry for a polydisperse polymer melt by combining the RDP and polySTRAND models. Implementing this model within the RheoTool within OpenFOAM required a number of key developments, including modifications to the underlying models. These are as follows:

1. Our reason for using the RDP model is that it accounts for interactions between polymers of differing lengths, which are not present in models that use a simple superposition of stress contributions. As a result, its linear rheology does not reduce to a simple superposition of one Maxwell modes per component but is instead given by double reptation. Hence, we needed to develop a procedure for mapping from a Maxwell mode fit to linear rheology data onto a discrete set of RDP model species. This was achieved via matching the modulus and viscosity of combinations of the Maxwell modes to determine the

corresponding volume fraction and reptation relaxation times of the RDP species.

- 2. Another challenge with the RDP model is that the number of constitutive variables increases with the square of the number of chain species, and since these evolution equations are coupled, they cannot be assembled using the existing multimode functionality in RheoTool. It was, therefore, necessary to find a way to automatically generate the constitutive equation code of the RDP model for a general number of chain species. This was achieved using a script that generates the RheoTool files for the RDP constitutive equations for *n* chain species.
- 3. The key parameter required from the RDP model to input into the polySTRAND model is a prediction of the bond orientation distribution $P_{2,K}$ from the configuration tensor. We found that the formula for obtaining $P_{2,K}$ used in the original polySTRAND model [34] was not consistent with finite extensibility of the chain, which meant that in a strong flow it was possible for $P_{2,K}$ to exceed unity. To resolve this, we provide a consistent calculation for $P_{2,K}$ using a similar approach to Li and Larson [50] but applied to entangled polymer melts.
- 4. Previously, the polySTRAND model had only been applied to spatially homogeneous flows [34]. Although it is computationally far less intensive than other coarsegrained methods that retain molecular detail, such as the GO model [31], it still requires three nested nonlinear numerical procedures: a solution of a nonlinear equation, which is performed at every point of a minimisation over the nucleus aspect ratio, all of which is finally maximized over nucleus size to find the nucleation barrier. Instead of performing this calculation at each point in space and time, we were able to increase the efficiency of our simulations by using a precalculated interpolation function, Eq. (19) for the nucleation rate as a function of Δf_i .
- 5. Having determined the rate of nucleation, the final part of the calculation is to calculate the growth of the crystallites from the Schneider rate equations [51]. A computational challenge here is that the nucleation rate depends exponentially on local changes in chain conformation free energy and can be highly localized resulting in large spatial gradients in the number and volume density of crystals. To mitigate numerical errors associated with advection, we used logarithmic functions of these quantities for calculating their evolution. This increases the numerical stability of our simulations.

As a demonstrator of this methodology, we considered flow-induced crystallization within the contraction expansion geometry considered by Scelsi et al. [41]. Our model predicts accurately the location of the crystallites, which are confined to highly localized "fangs" that result from material advected downstream from the high shear region near the wall of the contraction. This demonstrates that in this geometry it is shear rather than extension that induces the vast majority of the nucleation. Our simulations do, however, underestimate the flow rates required to observe crystallization relative to experiments. The exponential dependence of the rate of crystallization on free energy associated with chain configuration means this onset flow rate is very sensitive to model parameters whose values we do not know precisely, without further experiments.

The goal of our work is that such model parameters should depend only on the local chemistry of the material, i.e., the monomer type. Once these parameters are known, this modeling approach should be predictive of the effects of molecular weight, long-chain branching, and flow. While there are multiple such parameters required for a full description, the number is not so large to be beyond reach to determine these through experiment and simulation; we hope that this acts as a prompt for further investigation.

Further enhancements to this model would be to allow for variations in temperature and also to account for changes in melt rheology as a result of crystallization. In their model, Roozemond et al. [27] accounted for rheological changes through an empirical scaling of the modulus as a function of crystal volume fraction. More recently, Andreev and Rutledge [62] provided a slip-link model for a partially crystallized entangled polymer melt by introducing additional cross-links to represent molecules tied between developing crystallites. As well as changes to the rheology of the melt, there will also be compositional changes as longer chains will be disproportionately incorporated into crystallites, which will reduce their concentration within the melt phase.

SUPPLEMENTARY MATERIAL

See the supplementary material for details of (I) the fitting § of the Rolie-Double-Poly model to linear rheological data given by a set of Maxwell modes, (II) the polySTRAND & model calculation, and (III) the derivation of our new expression for the Kuhn segment orientation using the freely $\frac{\omega}{2}$ jointed chain model.

ACKNOWLEDGMENTS

W.P.G. acknowledges the funding given by EPSRC Center for Doctoral Training in Molecules to Product, Grant Ref. No. EP/S022473/1. The authors would like to thank Professor Richard Graham for very helpful discussions at many points during this work.

AUTHOR DECLARATIONS

Conflict of Interest

The authors have no conflicts to disclose.

DATA AVAILABILITY

The data that support the findings of this study are openly available in the Research Data Leeds Repository at https:// doi.org/10.5518/1581, Ref. [46].

REFERENCES

[1] Graham, R. S., "Understanding flow-induced crystallization in polymers: A perspective on the role of molecular simulations," J. Rheol. 63, 203-214 (2019).

- [3] Wang, Z.-B., Y.-M. Mao, X.-K. Li, Y.-G. Li, C. Jarumaneeroj, B. Thitisak, P. Tiyapiboonchaiya, W. Rungswang, and B. S. Hsiao, "The influence of ethyl branch on formation of shish-kebab crystals in bimodal polyethylene under shear at low temperature," Chin. J. Polym. Sci. 39, 1050–1058 (2021).
- [4] Seo, J., D. Parisi, A. M. Gohn, A. Han, L. Song, Y. Liu, R. P. Schaake, A. M. Rhoades, and R. H. Colby, "Flow-induced crystallization of poly (ether ether ketone): Universal aspects of specific work revealed by corroborative rheology and x-ray scattering studies," Macromolecules 53, 10040–10050 (2020).
- [5] Jacob, B. J., X. Zhang, J. Kim, J. D. Alexander, M. E. Cangussú, A. M. Rhoades, and R. H. Colby, "Particle concentration promotes flow-induced crystallization of high-molecular-weight isotactic polypropylene," Macromolecules 57, 4396–4409 (2024).
- [6] Zhao, R., Z. Chu, and Z. Ma, "Flow-induced crystallization in polyethylene: Effect of flow time on development of shish-kebab," Polymers 12, 2571–2582 (2020).
- [7] Nicholson, D. A., and G. C. Rutledge, "Molecular simulation of flow-enhanced nucleation in n-eicosane melts under steady shear and uniaxial extension," J. Chem. Phys. 145, 244903 (2016).
- [8] Nicholson, D. A., and G. C. Rutledge, "An assessment of models for flow-enhanced nucleation in an n-alkane melt by molecular simulation," J. Rheol. 63, 465–475 (2019).
- [9] Anwar, M., J. T. Berryman, and T. Schilling, "Crystal nucleation mechanism in melts of short polymer chains under quiescent conditions and under shear flow," J. Chem. Phys. 141, 124910 (2014).
- [10] Anwar, M., and R. S. Graham, "Molecular dynamics simulations of crystal nucleation in entangled polymer melts under start-up shear conditions," J. Chem. Phys. 150, 084905 (2019).
- [11] Jabbarzadeh, A., "The origins of enhanced and retarded crystallization in nanocomposite polymers," Nanomaterials 9, 1472–1485 (2019).
- [12] Jabbarzadeh, A., and B. Halfina, "Unravelling the effects of size, volume fraction and shape of nanoparticle additives on crystallization of nanocomposite polymers," Nanoscale Adv. 1, 4704–4721 (2019).
- [13] Anogiannakis, S. D., F. Venetsanos, and D. N. Theodorou, "Simulating stretch-induced crystallization of polyethylene films: Strain rate and temperature effect on the kinetics and morphology," Macromolecules 57, 7331–7346 (2024).
- [14] Nie, Y., J. Wen, Y. Ming, and Y. Zhou, "Mechanisms of flow-induced multistep structure evolution in semicrystalline polymers revealed by molecular simulations," Cryst. Growth Des. 24, 6531–6547 (2024)
- [15] Hussain, M. A., T. Yamamoto, S. F. Adil, and S. Yao, "Coarse-grained simulations on polyethylene crystal network formation and microstructure analysis," Polymers 16, 1007–1024 (2024).
- [16] Nie, Y., Y. Zhao, G. Matsuba, and W. Hu, "Shish-kebab crystallites initiated by shear fracture in bulk polymers: 2. crystallization on shearing," Polymer 274, 125909 (2023).
- [17] Nie, C., F. Peng, T. Xu, Y. Ding, J. Sheng, W. Chen, and L. Li, "Biaxial stretch-induced crystallization of polymers: A molecular dynamics simulation study," Macromolecules 54, 9794–9803 (2021).
- [18] Liu, Z., Z. Zhou, Y. Ming, S. Zhang, T. Hao, and Y. Nie, "Molecular dynamics simulations of nucleation details in stretched polyethylene," Polymer 195, 122442 (2020).
- [19] Ming, Y., Z. Zhou, J. Yang, T. Hao, and Y. Nie, "Stretching-induced nucleation and crystallization of cyclic polyethylene: Insights from molecular dynamics simulation," Eur. Polym. J. 173, 111232 (2022).

- [20] Anwar, M., and R. S. Graham, "Direct observation of long chain enrichment in flow-induced nuclei from molecular dynamics simulations of bimodal blends," Soft Matter 17, 2872–2882 (2021).
- [21] Nafar Sefiddashti, M. H., B. J. Edwards, and B. Khomami, "Atomistic simulation of flow-induced microphase separation and crystallization of an entangled polyethylene melt undergoing uniaxial elongational flow and the role of kuhn segment extension," Polymers 15, 1831–1867 (2023).
- [22] Hagita, K., T. Yamamoto, H. Saito, and E. Abe, "Chain-level analysis of reinforced polyethylene through stretch-induced crystallization," ACS Macro Lett. 13, 247–251 (2024).
- [23] Nafar Sefiddashti, M. H., B. J. Edwards, and B. Khomami, "Flow-induced phase separation and crystallization in entangled polyethylene solutions under elongational flow," Macromolecules 53, 6432–6451 (2020).
- [24] Nafar Sefiddashti, M. H., B. J. Edwards, and B. Khomami, "Flow-induced phase phenomena in an entangled polyethylene/ benzene solution under uniaxial elongational flow," Rheol. Acta 63, 113–133 (2024).
- [25] Doufas, A. K., I. S. Dairanieh, and A. J. McHugh, "A continuum model for flow-induced crystallization of polymer melts," J. Rheol. 43, 85–109 (1999).
- [26] Steenbakkers, R. J., and G. W. Peters, "A stretch-based model for flow-enhanced nucleation of polymer melts," J. Rheol. 55, 401–433 (2011).
- [27] Roozemond, P. C., M. van Drongelen, Z. Ma, M. A. Hulsen, and G. W. Peters, "Modeling flow-induced crystallization in isotactic polypropylene at high shear rates," J. Rheol. 59, 613–642 (2015).
- [28] McIlroy, C., and R. S. Graham, "Modelling flow-enhanced crystallisation during fused filament fabrication of semi-crystalline polymer melts," Addit. Manuf. 24, 323–340 (2018).
- van Berlo, F. P. A., R. Cardinaels, G. W. Peters, and P. D. Anderson, S. W. Peters, and P. D. W. Peters, and P. D. W. Peters, and P. W. Peters, and P. D. W. Peters, and P. W. Peters, and P
- [30] Verbeeten, W. M., G. W. Peters, and F. P. Baaijens, "Numerical simulations of the planar contraction flow for a polyethylene melt using the xpp model," J. Non-Newtonian Fluid Mech. 117, 73–84 (2004).
- [31] Graham, R. S., and P. D. Olmsted, "Kinetic monte carlo simulations of flow-induced nucleation in polymer melts," Faraday Discuss. 144, 71–92 (2010).
- [32] Graham, R. S., and P. D. Olmsted, "Coarse-grained simulations of flow-induced nucleation in semicrystalline polymers," Phys. Rev. Lett. 103, 115702 (2009).
- [33] Jolley, K., and R. S. Graham, "Flow-induced nucleation in polymer melts: A study of the go model for pure and bimodal blends, under shear and extensional flow," Rheol. Acta 52, 271–286 (2013).
- [34] Read, D. J., C. McIlroy, C. Das, O. G. Harlen, and R. S. Graham, "Polystrand model of flow-induced nucleation in polymers," Phys. Rev. Lett. 124, 147802 (2020).
- [35] Likhtman, A. E., and R. S. Graham, "Simple constitutive equation for linear polymer melts derived from molecular theory: Rolie–poly equation," J. Non-Newtonian Fluid Mech. 114, 1–12 (2003).
- [36] Boudara, V. A., J. D. Peterson, L. G. Leal, and D. J. Read, "Nonlinear rheology of polydisperse blends of entangled linear polymers: Rolie-double-poly models," J. Rheol. 63, 71–91 (2019).
- [37] Read, D. J., K. Jagannathan, S. K. Sukumaran, and D. Auhl, "A full-chain constitutive model for bidisperse blends of linear polymers," J. Rheol. 56, 823–873 (2012).
- [38] Ruan, C., "Kinetics and morphology of flow induced polymer crystallization in 3D shear flow investigated by Monte Carlo simulation," Crystals 7, 51–67 (2017).

0 October 2025 12:09:07

- [39] Pimenta, F., and M. A. Alves, "Stabilization of an open-source finite-volume solver for viscoelastic fluid flows," J. Non-Newtonian Fluid Mech. 239, 85–104 (2017).
- [40] Jasak, H., A. Jemcov, and Z. Tukovic, "Openfoam: A c++ library for complex physics simulations," in *International Workshop on Coupled Methods in Numerical Dynamics* (IUC, Dubrovnik, Croatia, 2007), Vol. 1000, pp. 1–20.
- [41] Scelsi, L., M. Mackley, H. Klein, P. Olmsted, R. Graham, O. Harlen, and T. McLeish, "Experimental observations and matching viscoelastic specific work predictions of flow-induced crystallization for molten polyethylene within two flow geometries," J. Rheol. 53, 859–876 (2009).
- [42] Azahar, A. A., O. G. Harlen, and M. A. Walkley, "Modelling contraction flows of bi-disperse polymer blends using the rolie-poly and roliedouble-poly equations," Korea-Aust. Rheol. J. 31, 203–209 (2019).
- [43] Warner, H. R., Jr., "Kinetic theory and rheology of dilute suspensions of finitely extendible dumbbells," Ind. Eng. Chem. Fundam. 11, 379–387 (1972).
- [44] Cohen, A., "A padé approximant to the inverse langevin function," Rheol. Acta 30, 270–273 (1991).
- [45] Des Cloizeaux, J., "Double reptation versus simple reptation in polymer melts," Europhys. Lett. 5, 437–442 (1988).
- [46] Grant, W., O. G. Harlen, and D. J. Read (2024). "Polydisperse data," University of Leeds. [Dataset] https://doi.org/10.5518/1581
- [47] Bishko, G., T. McLeish, O. Harlen, and R. Larson, "Theoretical molecular rheology of branched polymers in simple and complex flows: The pom-pom model," Phys. Rev. Lett. 79, 2352–2355 (1997).
- [48] Hamer, M. J., J. A. Wattis, and R. S. Graham, "A method to project the rate kinetics of high dimensional barrier crossing problems onto a tractable 1D system," Soft Matter 8, 11396–11408 (2012).
- [49] Dealy, J. M., D. J. Read, and R. G. Larson, Structure and Rheology of Molten Polymers: From Structure to Flow Behavior and Back Again (Carl Hanser Verlag GmbH Co KG, Munich, 2018).
- [50] Li, L., and R. Larson, "Excluded volume effects on the birefringence and stress of dilute polymer solutions in extensional flow," Rheol. Acta 39, 419–427 (2000).
- [51] Schneider, W., A. Koppl, and J. Berger, "Non-isothermal crystallization of polymers. System of rate equations," Int. Polym. Process. 2, 151–154 (1988).

- [52] Avrami, M., "Kinetics of phase change. II transformation-time relations for random distribution of nuclei," J. Chem. Phys. 8, 212–224 (1940)
- [53] Mattice, W. L., C. A. Helfer, and A. P. Sokolov, "On the relationship between the characteristic ratio of a finite chain, C_n , and the asymptotic limit, C_{∞} ," Macromolecules **36**, 9924–9928 (2003).
- [54] Matsuyama, H., K. Hayashi, T. Maki, M. Teramoto, and N. Kubota, "Effect of polymer density on polyethylene hollow fiber membrane formation via thermally induced phase separation," J. Appl. Polym. Sci. 93, 471–474 (2004).
- [55] Fetters, L. J., D. J. Lohse, S. T. Milner, and W. W. Graessley, "Packing length influence in linear polymer melts on the entanglement, critical, and reptation molecular weights," Macromolecules 32, 6847–6851 (1999).
- [56] Szántó, L., R. Vogt, J. Meier, D. Auhl, E. Van Ruymbeke, and C. Friedrich, "Entanglement relaxation time of polyethylene melts from high-frequency rheometry in the mega-hertz range," J. Rheol. 61, 1023–1033 (2017).
- [57] Martin, G. M., and E. Passaglia, "Density of polyethylene crystals grown from solution," J. Res. Natl. Bur. Stand. Sect. A Phys. Chem. 70, 221–224 (1966).
- [58] Zhou, H., and G. Wilkes, "Comparison of lamellar thickness and its distribution determined from d.s.c., SAXS, TEM and AFM for highdensity polyethylene films having a stacked lamellar morphology," Polymer 38, 5735–5747 (1997).
- [59] Yi, P., C. R. Locker, and G. C. Rutledge, "Molecular dynamics simulation of homogeneous crystal nucleation in polyethylene," Macromolecules 46, 4723–4733 (2013).
- [60] Hoffman, J. D., L. J. Frolen, G. S. Ross, and J. I. Lauritzen Jr, "On the growth rate of spherulites and axialites from the melt in polyethylene fractions: Regime I and regime II crystallization," J. Res. Natl. Bur. Stand. Sect. A Phys. Chem. **79**, 671–699 (1975).
- [61] Lee, K., M. Mackley, T. McLeish, T. Nicholson, and O. Harlen, Street "Experimental observation and numerical simulation of transient stress fangs' within flowing molten polyethylene," J. Rheol. 45, 1261–1277 (2001).
- [62] Andreev, M., and G. C. Rutledge, "A slip-link model for rheology of entangled polymer melts with crystallization," J. Rheol. 64, 213–222 (2020).